UCLouvain

epl

École polytechnique de Louvain

Modelling and simulation of immersed particle chains

Application to moving boundary problems

Authors: **Jimmy Fraiture, Clodagh Jevens**
Supervisors: **Jonathan Lambrechts, Vincent Legat**
Readers: **Miltiadis Papalexandris, Nathan Coppin**
Academic year 2020–2021
Master [120] in Mathematical Engineering
Master [120] in Mechanical Engineering

Abstract

Two enhancements are added to *MigFlow*, enabling us to tackle previously unachievable challenges. The first pertains to polymeric fluids and the second concerns moving boundaries.

Firstly, a polymer model is created using a scale analogy, highlighting the mechanisms responsible for the non-Newtonian behaviour of polymeric fluids. An adapted FENE model, as well as an implementation of Brownian motion, simulate the physical properties of polymers. Improved versions of the Dumbbell model are explored to compare their properties and uses.
Secondly, moving boundaries are required for a large range of problems in engineering and handling these, therefore, is of great importance. The proposed model is also valid for all finite element problems and is supported by multiple simulations.

The previous enhancements are used to implement two concrete applications: the journal bearing and the delayed die swell. The simulation of the journal bearing is validated and is in agreement with numerical and experimental data. Subsequent studies show the influence of polymeric fluids on these results. Additionally, our simulations prove relevant for many types of industrial applications.
The simulation of the delayed die swell uses a multi-scale approach to understand this complex phenomenon, bringing attention to the behaviour of polymers and bridging the gap between micro and macro scales.

Acknowledgements

We wish to express our appreciation to the *MigFlow* team for their unwavering guidance and advice throughout the year. We are extremely grateful to have been part of this project.

In particular, we would like to extend our sincere thanks to: Vincent Legat for his help in rheology and fluid modelling, Jonathan Lambrechts for his expertise in the *Migflow* code and numerical simulations, Nathan Coppin and Michel Henry for their availability and help throughout the whole year.

We also wish to thank our respective families for their unconditional support and patience, not only during this past year but over these last five years in university. Additional thanks to the Jevens family for their help during the correction of the thesis.

Contents

List of Symbols

Symbol	Description	Units
Polymer modelling		
$\boldsymbol{\Delta x}$	Displacement	$[m]$
$\boldsymbol{R}$	Vector between 2 particles	$[m]$
ε	Boundary layer size of the adapted FENE model	$[m]$
k	Stiffness of elastic body	$[\frac{N}{m}]$
Q	Maximum elastic extension	$[m]$
Adaptive mesh		
$\boldsymbol{\Delta d_A}$	Displacement of one point of the boundary	$[m]$
$\boldsymbol{\Delta d}$	Displacement of the whole boundary	$[m]$
P	Set of point of the mesh	$[-]$
p	Coordinates of an arbitrary point of the mesh	$[m]$
p'	New coordinates of an arbitrary point of the mesh	$[m]$
Journal Bearing		
Λ	Sommerfeld number $\Lambda = \frac{6 \cdot \mu \cdot \omega}{C^2}$	$[-]$
ω	Rotational speed of the journal	$[rpm]$
ϕ	Attitude angle	$[-]$
ρ	Density of the fluid	$[kg/m^3]$
ζ	Loading parameter $\zeta = \frac{W}{2 \cdot r \cdot P_a}$	$[-]$
c	Clearance $c = R_{out} - R_{in}$	$[m]$
e	Eccentricity	$[-]$
r	Dimensionless radius of the journal $r = \frac{R_{in}}{R_{out}}$	$[-]$

R_{in}	Radius of the journal	$[m]$
R_{out}	Radius of the outer bearing	$[m]$
W	Load of the journal	$[N]$

Delayed die swell

d	Diameter of the tube	$[m]$
D_1	Diameter of the fluid after the first swell	$[m]$
D_2	Diameter of the fluid after the second swell (delayed)	$[m]$
L	End of the second swell (delayed)	$[m]$
l	End of the first swell	$[m]$

List of Figures

Chapter 1

Introduction

This document is based on *MigFlow*[1], an open-source software used to simulate immersed granular flows. *MigFlow* (**M**odel for **I**mmersed **G**ranular **Flow**s) is the result of a collaboration between the Université Catholique de Louvain and the Université de Montpellier. It uses a multi-scale approach to analyse the behaviour of every grain that is immersed in the fluid and its impact on the flow. The system is used to simulate various applications such as a fluid injection in a granular mix, grain sorting using water jigging, dam breaks and many more.

MigFlow's software is composed of a fluid solver that simulates the fluid phase and a particle solver to handle the granular phase. The fluid phase is solved using a coarse-scale finite element method that solves the Navier-Stokes equations [1]. This method assumes the flow is incompressible and, as such, only the pressure and velocity fields are calculated. The granular phase uses an iterative position and contact solver. This prevents particles from penetrating one another or the boundaries and simulates the frictions between the different materials. Using both solvers enables us to understand and simulate interactions between the fluid and the particles. This is done by calculating the particle distribution across the domain.
The software is also capable of handling both Dirichlet and Neumann boundary conditions as well as multiphase fluid flows. It is important to note that *MigFlow* requires all particles to be considerably smaller than the elements of the mesh.

For this thesis, the opportunity arose to research and implement enhancements to *MigFlow*. At present, the software is limited to incompressible Newtonian fluids. Our first contribution is to include the ability to handle non-Newtonian fluids. We do so by defining a polymer model based on *Migflow*'s grains. Introducing these polymers into the fluid results in a non-Newtonian fluid. This method allows us to simulate these fluids without having to use constitutional equations such as the Oldroyd-B model.

Non-Newtonian fluids are of great importance in everyday life and can be found in an array of products such as soaps, toothpaste, cosmetics, paints, etc. They have a vast number of usages across multiple fields and industries, for example, the automotive industry (for lubricants) and life sciences (as blood is a non-Newtonian fluid).
The polymer chains we simulate are implemented using a scale analogy. Each polymer chain represents a set of microscopic polymers but behaves in the same way as a single microscopic polymer. This enables us to use a reasonable amount of polymers while observing non-Newtonian

[1] `www.migflow.be`

behaviours at a macro-scale. Additionally, it allows us to follow the evolution of these polymer chains and observe their interactions with the fluid.
Within the finite element method used to solve the fluid phase, we have added our second enhancement to allow for the adaption of the mesh according to moving boundaries. This is an important feature as many problems require dynamic geometries. We will propose a method that does so while maintaining a correct solution using the new or adapted mesh. This makes it possible to simulate more complex systems and we shall discuss several examples throughout this document.

This master thesis is divided into four main parts. The first, (Chapter 2) is devoted to the development and implementation of immersed polymers. The chapter begins with a brief reminder of the underlying physics of polymers and polymeric fluids. Using a mesoscopic scale makes it possible to simulate a reasonable amount of chains and decrease computational costs while still observing non-Newtonian behaviours. We will explore different possible structures and apply our polymers to a simple shearing problem.

Chapter 3 focuses on moving boundaries in which we implement a method that is valid for 2D finite element problems and is supported by multiple simulations. We briefly discuss the application of this method to simulate a magnetic stirrer.

Once these tools have been implemented, we focus on the simulation and analysis of two practical cases using our previously described improvements: the journal bearing and the delayed die swell.

Chapter 4 is therefore dedicated to the study of the journal bearing. We review the state of the art and the physics that drive the bearing. Our simulations are validated by comparing our results to scientific researches. Various studies are then carried out to illustrate the pertinence of our simulations.

Finally, Chapter 5 explores the complex phenomenon called the delayed die swell in which we use a multiscale approach to gain a deeper understanding of its causes. We start by reviewing the underlying physics of the problem before developing simulations using the previously described polymer representation. This provides insights that help us highlight parameters that affect the swell and enables us to perform several analyses.

Chapter 2

Modelling polymers

Polymers, also called *macromolecules*, are made up of repeating units of atoms known as *structural units* or monomers. They may be linear or branched chains, sometimes forming 3D networks which give them various behaviours. Some are flexible and can be easily deformed like rubber and polyesters, while others are hard and tough like epoxies. Their abundance in nature, non-negligible physical and chemical effects make them interesting to study. Examples of naturally occurring polymers include proteins such as silk and collagen, DNA, polysaccharides and many more. They are used in numerous engineering applications such as the development of new generation solar cells [2], the study of protein properties [3], the storage or production of energy in molten salts [4] [5], tissue engineering [6] etc.

Polymers are also important facets of *rheology*, the study of the deformation and flow of matter. The field of rheology deals with, among other things, *non-Newtonian fluids* characterised by their non-respect of Newton's law of viscosity. The viscous behaviours of these fluids change depending on the stresses applied to them. In the specific case of *polymeric fluids* (polymer melts or solutions), we see contradicting behaviours: they present both viscous and elastic properties. This will be discussed in further detail throughout this chapter.

Our first contribution to the Project focuses on the inclusion of immersed polymers into the *MigFlow* software. This enables us to understand the mechanisms responsible for the non-Newtonian behaviour of polymeric fluids. Our polymer chains are created using a scale analogy, where each chain represents a set of microscopic polymers and assumes that these chains have the same properties as a single polymer. By doing so, we can simulate a larger range of experiments and applications. We will use the *MigFlow* particles and join them together using carefully chosen joints, where each joint represents a section of the chain.

To simulate the behaviour of these polymers and their impact on a fluid, we must be able to represent their *viscoelastic behaviour* and their *structural arrangement*. As the fluid is responsible for the *viscous* properties, we will start by describing two elastic models for the joints: one using Hooke's law and a second taking into account the maximum extension of a chain. Next, we will discuss two possible structures with different advantages and varying scopes. The benefits of each will then be explored before concluding with a practical application to demonstrate potential uses.

2.1 Physics of polymers and polymeric fluids

Before detailing how we implemented these polymers, it is essential to review the underlying physics of the problem.

As the name suggests, polymeric fluids contain polymers which results in interesting viscoelastic properties. The notion of elasticity may seem strange when speaking of fluids but this allows us to describe the complex phenomena observed. When polymers are subjected to a constraint, their configuration changes accordingly and when that constraint is lifted, they strive to regain their original shape. However, due to the interactions between the polymers and the fluid, this is not instantaneous. The polymeric fluid depends on past variables. We must therefore introduce the notion of *fading memory*. This is a term often used in mechanics to describe a material that is affected by past stresses and strains. Past events will have less influence on their behaviour than more recent ones.

Furthermore, as polymeric fluids are *non-Newtonian*, their viscosity is shear rate dependant:

$$\tau(t) = \mu(\dot{\gamma}(t))\ \dot{\gamma}(t) \tag{2.1}$$

where τ is the shear stress, $\dot{\gamma}$ is the shear strain rate and μ is the apparent viscosity.

Non-Newtonian fluids have some surprising responses to stress. There are two types with opposing behaviour: shear-thinning and shear-thickening. The viscosity of shear-thinning fluids (such as blood or paint) *decreases* as the shear rate increases. On the contrary, the viscosity of shear-thickening fluids (such as corn starch) *increases* with shear rate.

The structures of polymers are relevant in understanding their behaviour. As we can see in Figure 2.1, polymers can be arranged in different structures: linear chains, branched chains and networks. However, the latter are rarely present in liquid phases and will not be considered for this project (see Figure 2.1).

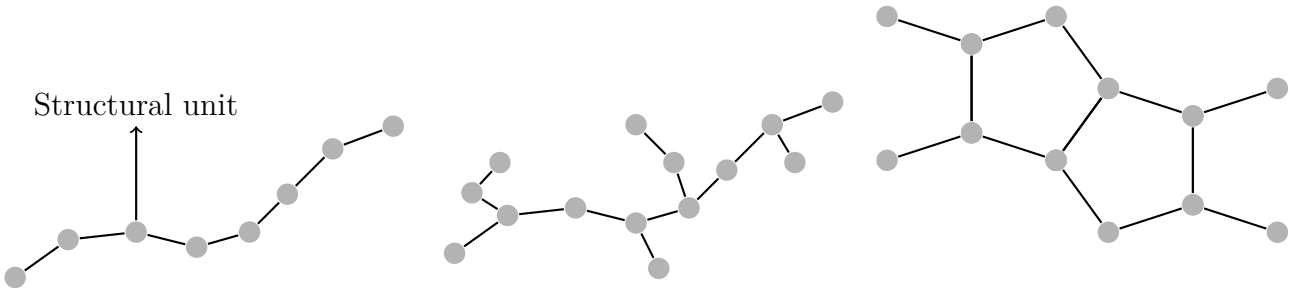

Figure 2.1: Structural arrangements of polymers (left - linear, centre - branched, right - network).

It is also important to note that structural units differ between natural and synthetic polymers. Most synthetic polymers are made up of a single structural unit and are referred to as *homopolymers*, while natural polymers are composed of many blocks. We call these *copolymers* and they may be arranged randomly, sequentially or form blocks (see Figure 2.2).

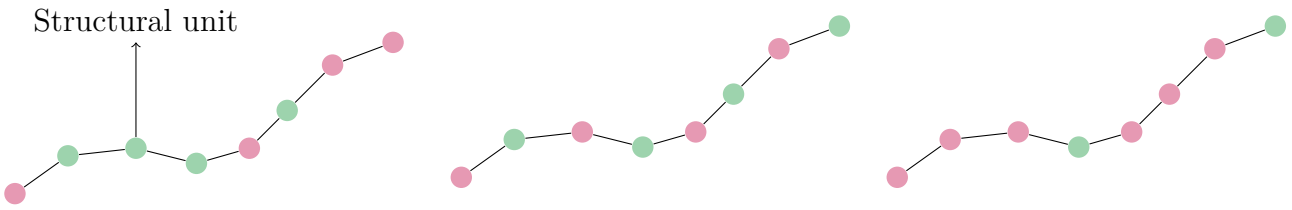

Figure 2.2: Arrangement of copolymers, the different colours represent different structural units (left - random, centre - sequential, right - block).

Immersed polymers are in a constant state of motion due to *random collisions* with fluid molecules. To simulate these collisions, a *Brownian force* is applied to each polymer [7]. These collisions give the initial energy necessary for the polymer to modify its shape, causing it to curl and maximise its entropy [8]. The implementation of this behaviour is described in Section 2.3.1.

Many experiments highlight these behaviours, for example, the *delayed die swell*. When a non-Newtonian fluid is extruded, the normal forces applied to the fluid change, causing it to swell. This phenomenon is discussed in further detail in Chapter 5.

2.2 Elastic model

As stated previously, it is vital to choose an appropriate elastic model for the joints. In doing so, we analysed two models. The first is a simple and well-known model based on Hooke's law. The second is the FENE model which proposes a solution to a limitation of Hooke's law i.e. the finite extension properties of bodies.

Please note that these elastic joints introduce new forces into *MigFlow*'s contact solver to account for interactions between neighbouring particles of a chain.

2.2.1 Hooke's law

Hooke's law[9], introduced by Robert Hooke in 1676, describes solids by stating that the elastic deformation is linearly proportional to the constraint. Formally, we can express this as follows:

$$\mathbf{F} = -k\mathbf{\Delta x} \tag{2.2}$$

where $\mathbf{F}$ is the force vector applied to the solid, k the stiffness of the body and $\mathbf{\Delta x}$ the deformation.

A well known application of Hooke's law is the *Hookean dumbbell model* which is a basic representation of a polymer, illustrated in Figure 2.3. The particles represent either end of the polymer while the spring joining them represents the polymer [10].

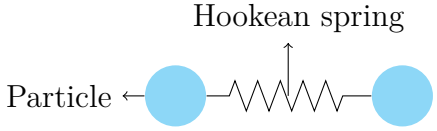

Figure 2.3: Illustration of the dumbbell representation.

In practice, this law is widely used due to its simplicity despite only being considered accurate for relatively small deformations around equilibrium (see appendix A). However, it does not take into account the maximal extension of the solid, which is vital in the case of polymers.
This limitation motivates us to search for something more appropriate such as the *FENE model*.

2.2.2 Finitely Extensible Nonlinear Elastic model (FENE model)

Contrary to Hooke's law, the *FENE model* [11] takes into account the maximum distance between two particles. Rather than a linear relationship between $\boldsymbol{F}$ and $\boldsymbol{\Delta x}$, the force tends to infinity as the deformation reaches the maximum extension, preventing us from exceeding it.

This model using the inverse of the Langevin function[1] is then used on the interval $[0; Q]$ where Q is the maximum extension. This gives a new expression for the force acting on the joint between two particles separated by a vector $\boldsymbol{\Delta x}$:

$$\boldsymbol{F} = \frac{k\ \boldsymbol{\Delta x}}{1 - (\frac{||\boldsymbol{\Delta x}||}{Q})^2} \tag{2.3}$$

As shown in Figure 2.4, the FENE model is in agreement with Hooke's law for small deformations (for which the physical validity is confirmed) while also preventing particles from straying too far from one another.

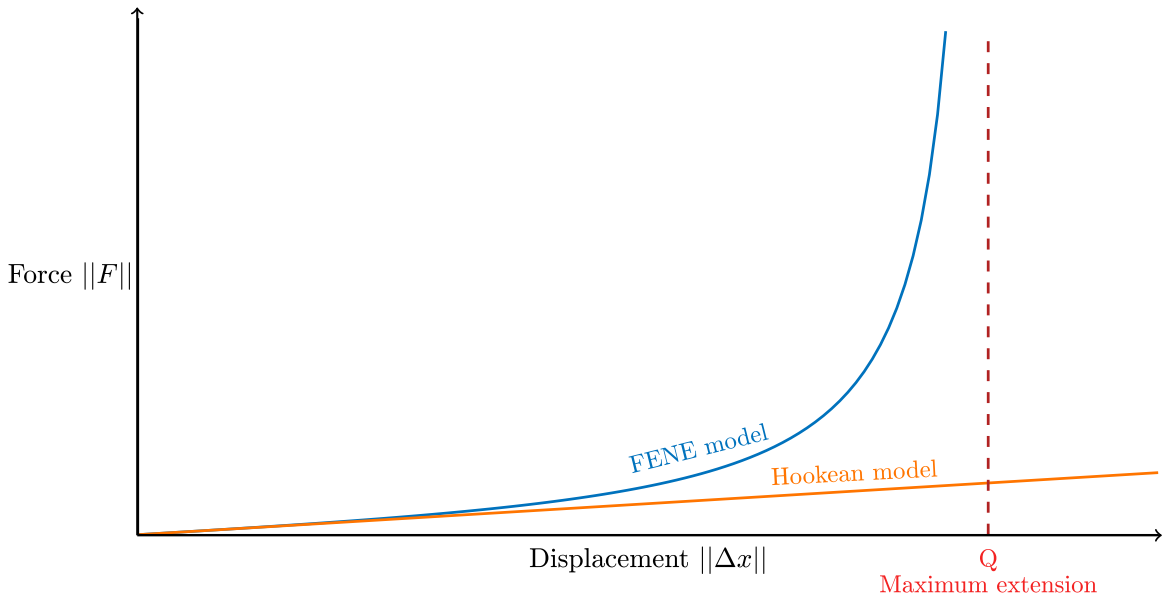

Figure 2.4: Comparison of the FENE model and the Hookean dumbbell model.

[1]Langevin function is defined as $L(x) = \coth(x) - \frac{1}{x}$

Adaptation for numerical simulation

The FENE model is not adapted for numerical simulations and therefore multiple steps must be taken to remedy this.

First, as we are working with a discrete time scale, it is possible to exceed the limit Q within a single time step and this is not acceptable. Mathematically, exceeding the limit creates a force of repulsion between the particles as: $||\boldsymbol{F}|| = \frac{k\ ||\boldsymbol{\Delta x}||}{1-(\frac{||\boldsymbol{\Delta x}||}{Q})^2} < 0$ if $||\boldsymbol{\Delta x}|| > Q$.

Secondly, this function tends to infinity as the maximum extension is reached. This would cause the simulation to crash if an excessively large number is considered by the solver. To overcome this issue, we have to consider an adaptation of the mathematical model (Equation 2.3). We achieve this by defining a small region ε around Q below which we will not exceed the limit in the next time step. Thus, for a fixed time step, the value of ε is chosen according to the velocity of the particles and the stiffness of the joint. It, therefore, depends on the Reynolds number of the fluid that carries the particles and k. An illustration of this function can be seen in Figure 2.5

These adjustments weaken the *finite extension* property as we no longer tend to infinity but the results remain valid and we maintain accurate solutions in the case of small deformations.

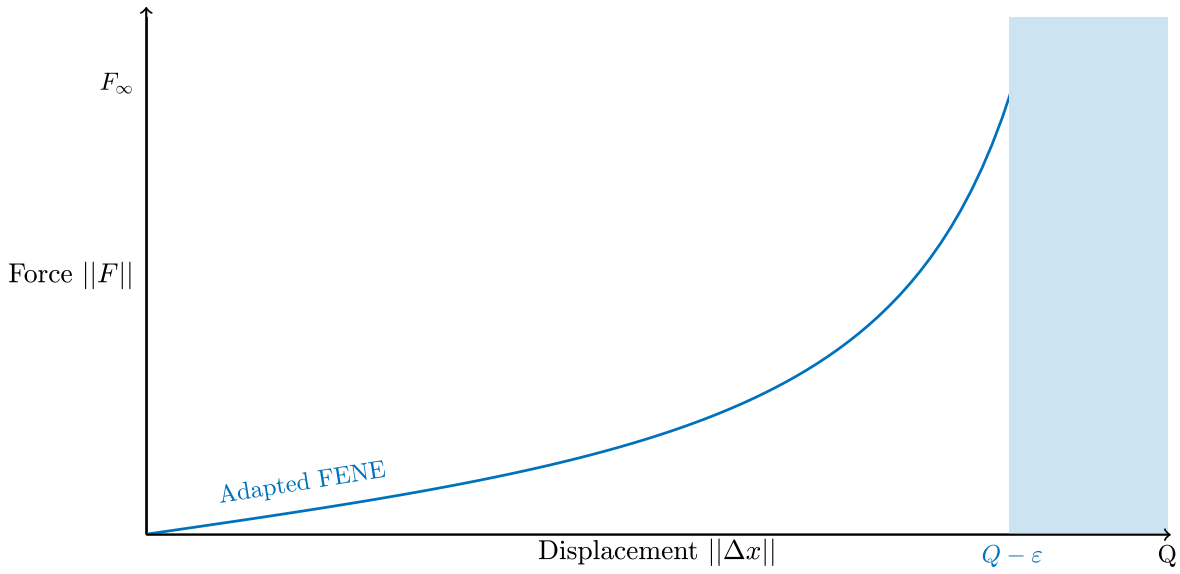

Figure 2.5: Illustration of the adapted FENE model.

A straightforward numerical experiment enables us to see the impact of our modifications on the FENE model. Furthermore, using this simple set-up makes it possible to observe the limits of the adaptation and prove it respects the conditions we have imposed.

Numerical experiment

This experiment, illustrated in Figure 2.6, ensures that our adapted model verifies the maximum extension property. We are studying a single joint, between two particles, one of which is fixed while the other is free to move vertically. We will apply a force to the free particle and observe the oscillatory behaviour. The results of this experiment are shown in Figure 2.7, where we compare Hooke's law and the adapted FENE model for small and large deformations.

In the case of small deformations, both behave in similar fashions. The difference becomes significant in the case of large deformations. The FENE model never crosses the maximal extension (represented by the dashed red line) contrary to Hooke's law. This means the maximum extension is respected for the adapted FENE model, confirming its validity. We therefore choose to move forward with this model.

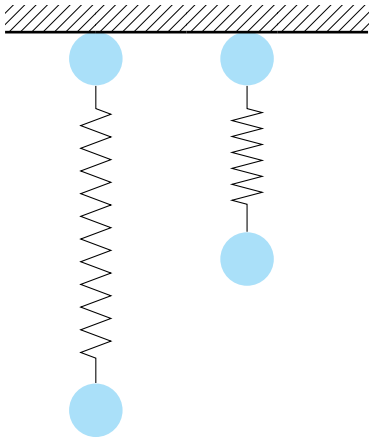

Figure 2.6: Illustration of the numerical experiment.

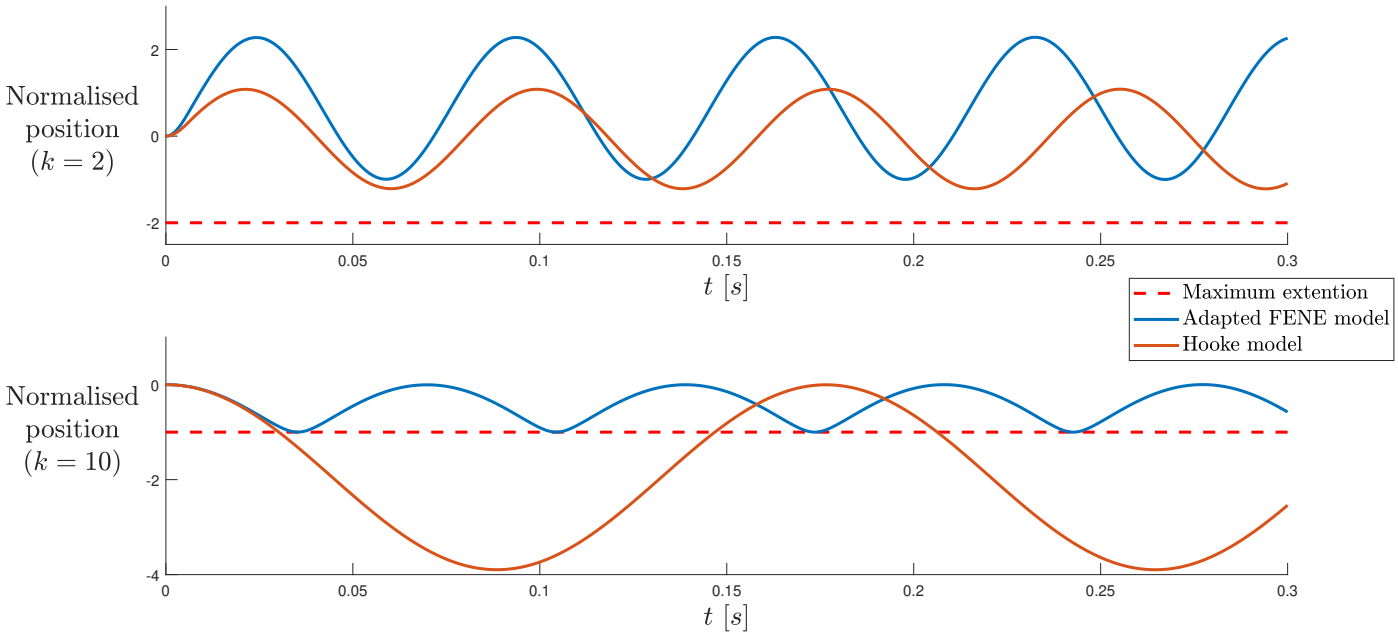

Figure 2.7: Normalised position of an oscillating particle with a Hooke spring (orange) and a FENE spring (blue). The first case is for k=2 and the second for k=10.

2.3 Polymer structures

Having chosen an elastic model, we move on to choosing a structure for our polymers. We are limiting ourselves to 2D cases and chain polymers.

2.3.1 Chain representation

Our first approach considers polymers made of rigid segments connected to a point and are free to rotate about this point. This representation (dubbed the *chain representation* and illustrated in Figure 2.8) is a concatenation of several dumbbell representations. This results in a more complex version of the dumbbell model.

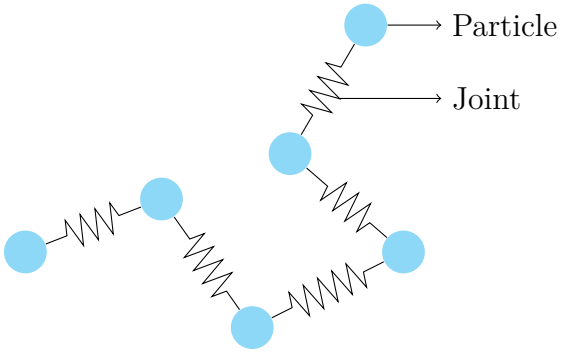

Figure 2.8: Illustration of the chain structure using springs.

Though this representation does not preserve the initial shape once external forces have been removed, it is particularly well-adapted for large scale problems. The stiffness of the joints for this representation is chosen according to parameters e.g. the temperature.

Brownian motion

Random collisions between polymers and fluid molecules force the polymer chains to curl when no external forces are applied [8]. At a micro time scale, this may be represented by Brownian forces that are purely random and uniformly distributed along the polymer. However, since we are working with a larger time scale (mesoscale), we consider an average force over several time steps. This results in a force directed to the centre of mass of the polymer (with an added Gaussian noise) [12] and reproduces the natural behaviour of the immersed polymers. This causes the polymer chains to curl and maximise their entropy.

The angle and intensity of the Brownian force applied to each particle is as follows:

$$\text{Angle of Brownian force: } \measuredangle \boldsymbol{F}_B^{(p)} \sim \mathcal{N}\left(\overline{\measuredangle\left(\boldsymbol{x}^{(p)}, \boldsymbol{C_M}\right)},\ \sigma^2_{angle}\right)$$
$$\text{Intensity of Brownian force: } ||\boldsymbol{F}_B^{(p)}|| \sim \mathcal{N}\left(\mu, \sigma^2\right)$$

where $\boldsymbol{x}^{(p)}$ is the position of the particle and $\boldsymbol{C_M}$ the position of the centre of mass of the polymer. The average intensity and variance of the force (μ, σ^2), as well as the variance of the noise (σ^2_{angle}), must be chosen according to the simulation parameters.

Influence on *MigFlow*

As a reminder, the aim of our first contribution to the *MigFlow* project is to assess the interactions between polymers and the fluid they are submerged in. We know a Newtonian fluid can be fully modelled with only a constant density and viscosity [13]. The addition of polymers (simulated using the chain representation) introduces an elastic component, impacts the effective viscosity of the fluid and impacts the Newtonian nature of the fluid.
In order to confirm the non-Newtonian behaviour of this polymeric fluid, we developed a simple case study. Let's consider a rectangular domain containing a steady-state shearing. At a given time $t = 0.0995s$, polymers are introduced in the fluid (evenly distributed over the whole domain). The effective viscosity can be measured numerically in the simulation. We see the evolution of this in Figure 2.9.

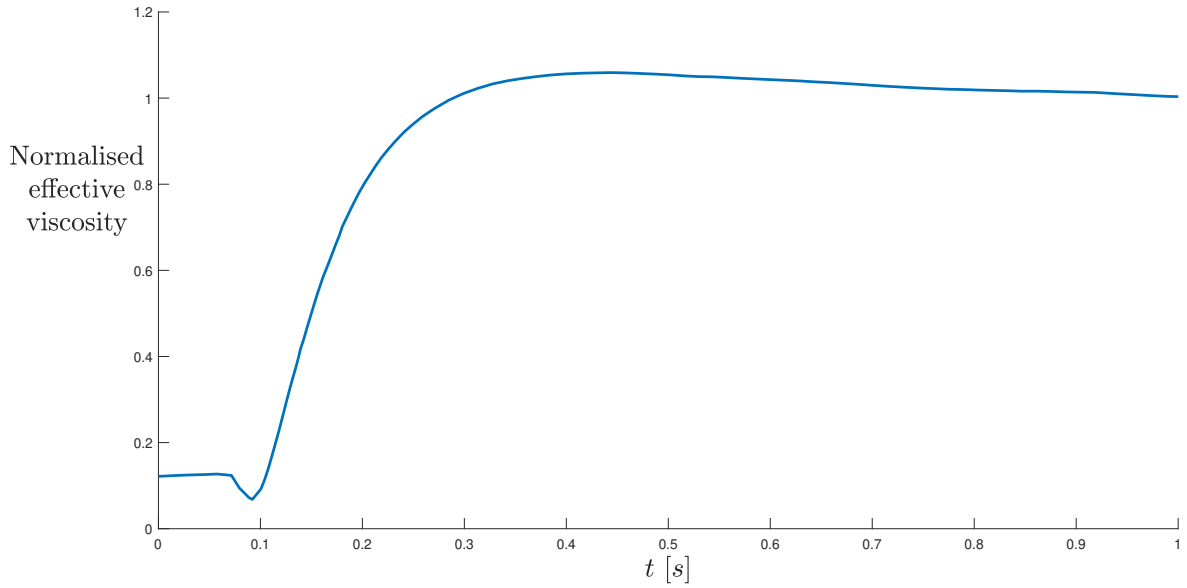

Figure 2.9: Effective viscosity of a shearing system according to time using 8 polymers (each of which contains 400 particles) in a chain representation.

A drop in the effective viscosity caused by the polymers being introduced in the domain is observed. A hypothesis is that this drop is due to the recomputation of the porosity over the whole domain. Then, the effective viscosity increases and an overshoot is observed which corresponds to the alignment of the polymers on the stream-line of the fluid. This overshoot is not described by Newton's law of viscosity and is typical behaviour of non-Newtonian fluids [14].
When the polymers are finally aligned, the viscosity stabilises and results in a higher viscosity value than without the polymers.

2.3.2 Triangular representation

The second approach covered in this chapter is a triangular representation.

This representation is intuitively based on the structure of molecular arrangement in 2D[2]. To conform with this arrangement, an angle of 120° must be maintained between two neighbouring particles at rest. This angle maximises the distance between each neighbouring particle.
When an external force is applied, this angle will vary accordingly, deforming the length and shape of the chain. Naturally, when the external force is no longer applied, the polymer tends to regain its initial shape.
In practice, the triangular representation consists of adding so-called *ghost particles* that are much lighter and smaller than the others to prevent any influence on the system. In so doing, we create a triangular network that allows us to achieve the desired angle and flexibility (see Figure 2.10). We will distinguish two types of spring: chain springs and shape springs. The chain springs are responsible for the elongation of the chain while the shape springs preserve the initial shape of the polymer.

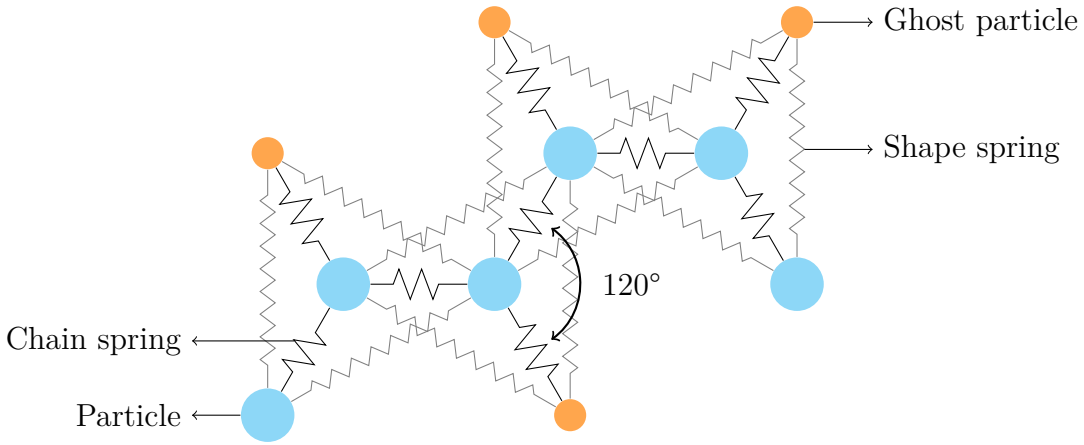

Figure 2.10: Illustration of the triangular representation.

This approach simulates the shape of a polymer and its tendency to recover when no stress is applied. The addition of *ghost particles* allows us to achieve this without needing rotational springs which are not well-defined for a full rotation and may be numerically unstable.

A drawback of this method is that it adds more particles to the simulation. It is not necessary to include these in the solvers since they do not influence the fluid nor collide with any of the other particles. As it is the position that is important, this must be tracked and updated according to the external forces being applied (joint constraints, fluid impact and Brownian motion). For a polymer composed of n particles, $n-2$ *ghost particles* are added to the system. The position update is computed in $\mathcal{O}(n)$, which does not impact the global complexity which is higher (at least $\mathcal{O}(n^2)$).
An example of a polymer with this structure is presented in Figure 2.11.

[2]based on the 2D projection of a tetrahedral arrangement [15]

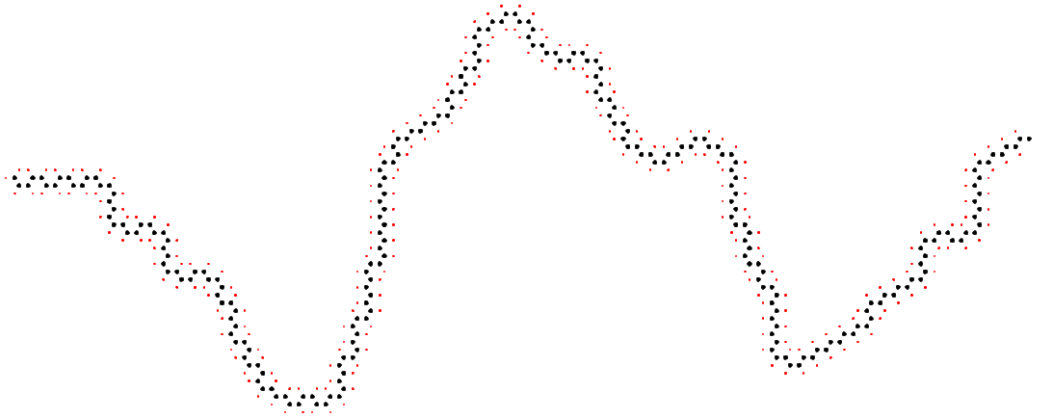

Figure 2.11: Example of a polymer of 500 particles with the triangular representation. The black points are particles and the red points are *ghost particles*.

Influence on *MigFlow*

The effective viscosity is measured in the same way as in the previous section.

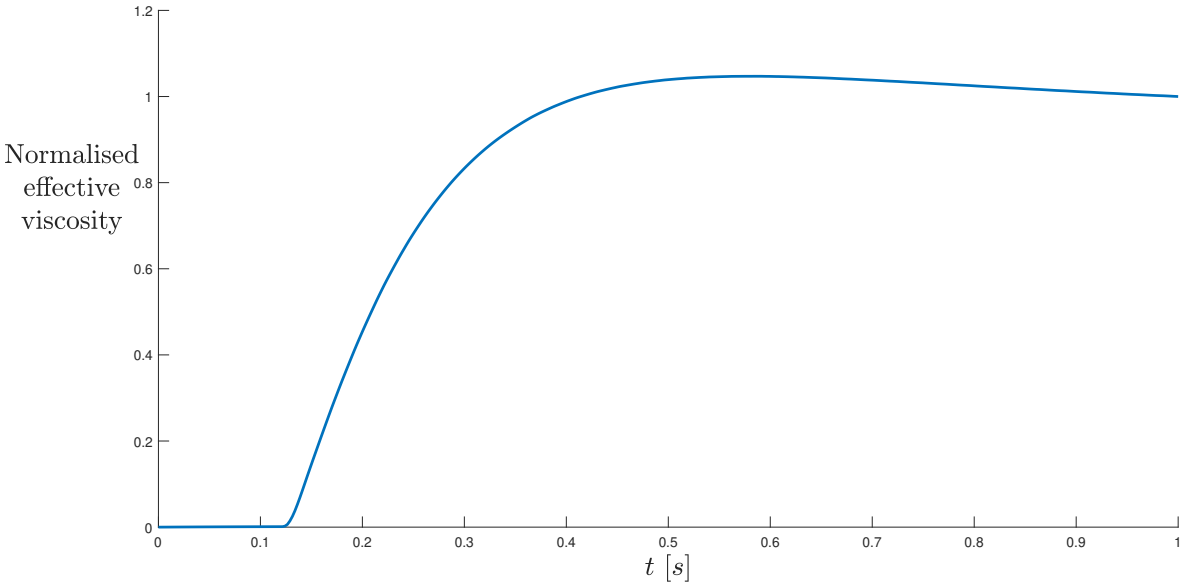

Figure 2.12: Effective viscosity of a shearing system according to time using 8 polymers (each with 400 particles) in a triangular representation.

The same increase in the effective viscosity is observed when polymers are added. We also see the typical overshoot of non-Newtonian fluid in Figure 2.12 just as in Figure 2.9.
A different injection method is used and we can avoid recomputing the porosity of the system. This means we no longer have a drop when the polymers are introduced to the system.

The influence on the fluid is the same as that of the chain representation which confirms that both representations have the same macroscopic properties. An overshoot is also observed and confirms the non-Newtonian nature of the resulting solution.

2.4 Comparison of the two models

The chain and the triangular representations contain certain parameters that must be modified according to the specific application. In this section, we demonstrate the typical behaviours of both.
We study the reactions of each case when polymers are introduced into a shearing flow and when the flow is stopped.

2.4.1 Chain representation

As stated previously, this representation does not preserve the initial shape of a chain.
At the beginning, the polymer is very condensed. As the shearing starts, the flow exerts a force on the chain, causing it to align with the streamlines. The joints use the adapted FENE model which allows the polymer to have a maximum extension and prevents particles from straying too far from their neighbours. When the fluid stops, the Brownian motion deforms the polymer and it curls back into a dense form with a different shape from the initial one (see Figure 2.13).

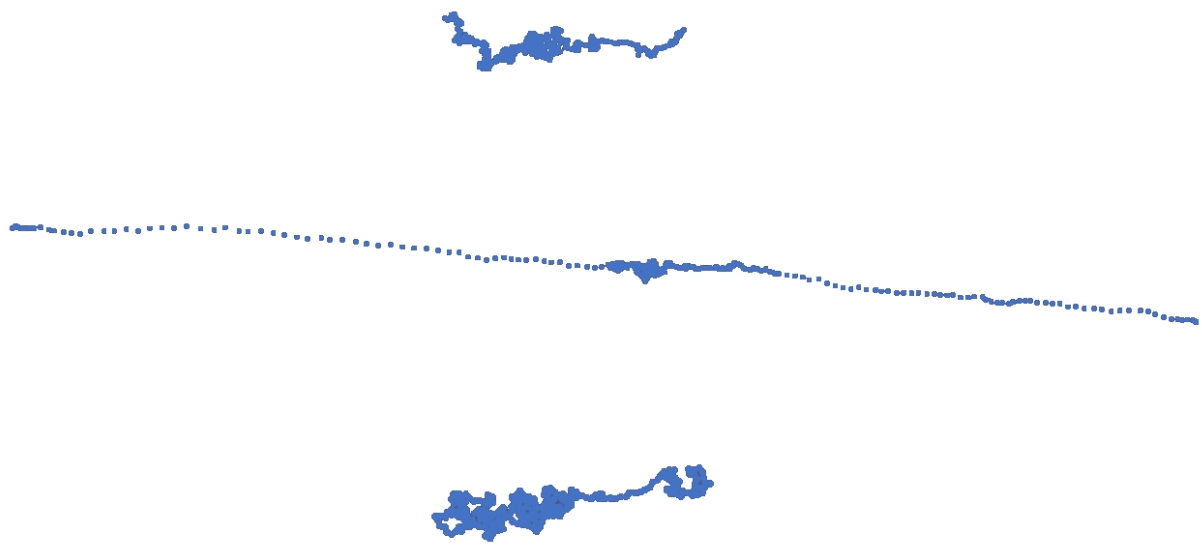

Figure 2.13: Evolution of a polymer : 1- initial state, 2- apply a deformation with a shearing, 3- new position due to Brownian motion.

This is in agreement with observations made in reality for large polymers at the macro-scale. Large polymers tend to minimise their extension to maximise their entropy [16] but do not preserve a fixed shape due to their size.

2.4.2 Triangular representation

The same experiment has been conducted on the triangular representation and the results are shown in Figure 2.14.

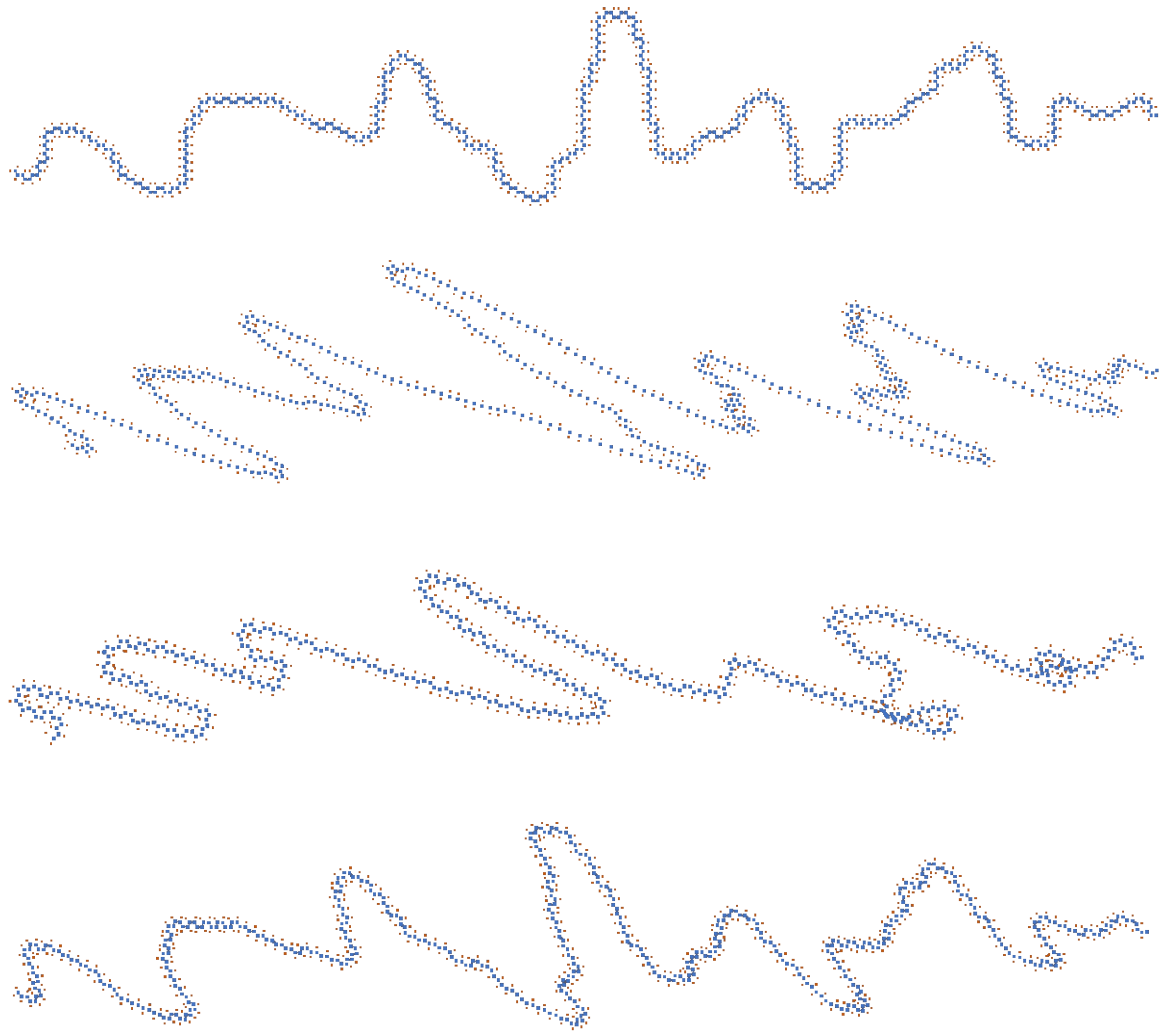

Figure 2.14: Evolution of a polymer : 1- initial state, 2- apply a deformation with a shearing, 3- regaining its shape, 4- new stable state

Similarly to the chain representation, the polymer is deformed by the fluid and tends to align with the streamlines. However, when the fluid stops, the polymer attempts to recover its original shape. Even if, in the end, the shape of the polymer is not exactly the same, it is an approximation of the initial shape. This illustrates the *memory* properties of viscoelastic bodies such as immersed polymers.

Discussion

Having compared both models, a summary of the main differences is shown in Table 2.1.

Feature	Chain representation	Triangular representation
Shape conservation	No	Yes
Polymer length	Long	Short
Stable	Yes	Yes
Deterministic	No	Yes
Initialisation	Random Walk	Random pattern

Table 2.1: Comparison of the characteristics of both representations.

The chain representation fits better for larger scale problems due to their physical properties and the number of particles needed. However, it doesn't preserve the initial shape of the polymer and uses a non-deterministic Brownian motion.
On the other hand, the triangular representation is more precise for small scale polymers. It preserves the initial shape as its representation is based on the real structure of polymers.

The structure of the polymer chains may be chosen according to the desired application.

2.5 Application of polymers in a shearing problem

To understand the interactions between the polymers and the fluid, we study the impact on a simple fluid mechanics problem.

2.5.1 Problem description

We are considering a 2D Couette-flow [17] between two parallel plates of infinite length. A constant velocity is applied to one plate while the other is stationary. Assuming non-slip conditions at the boundaries, meaning that there is no relative velocity between the fluid and the solid, we have a linear velocity profile.

The problem, along with the boundary conditions on the rectangular domain, are shown in Figure 2.15.

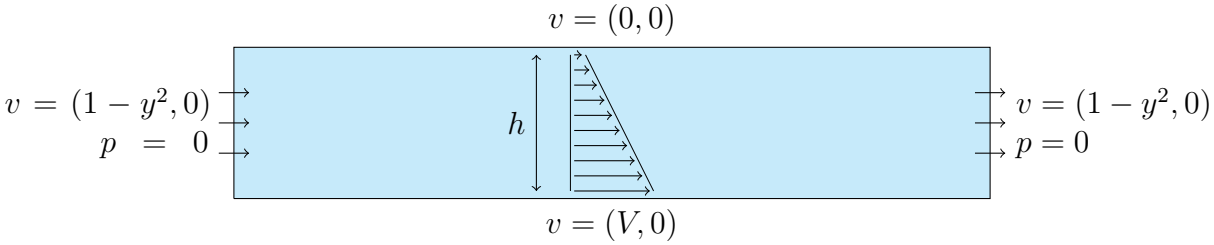

Figure 2.15: Shearing problem with boundary conditions and velocity profile (where V is non-dimensional).

An infinite domain is impossible to simulate with numerical tools. By applying periodic boundaries on a rectangular domain, it is sufficient to consider a period of the infinite domain without loss of generality. To achieve this, we consider that the velocity is the same on the left and right boundaries.

Information concerning the pressure also has to be provided to the *MigFlow* software in order to get a well-posed problem. This is done by specifying the mean pressure of the whole domain. After a short amount of iterations, the flow converges to a steady state solution as seen in Figure 2.16.

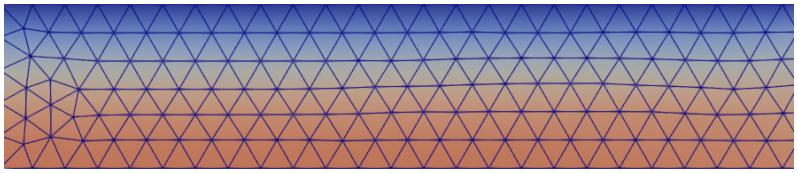

Figure 2.16: Solution of the x-velocity field in a steady state shearing (Red: $v_x = V$, Blue: $v_x = 0$, where V is non-dimensional).

The solution is regular, which confirms the periodic behaviour of the problem.

Since the goal of these simulations is to observe polymers in the domain, the periodic boundary conditions have to be defined for these chains. When a particle reaches the end of the domain, its position is relocated to the opposite side (with a small margin). In doing so, we prevent inter-particle penetration and preserve the density of the particles. The joints between particles must be treated individually to take into account the fact that a section of the chain may have already been relocated while another may not.

2.5.2 Simulation with polymers

Finally, polymers can be added to this shearing problem. We have chosen to use the chain representation as described in section 2.3.1. The goal of the simulation is to observe the interactions between the polymers and the fluid[3].

In theory, polymers, or any sufficiently flexible chain of elements, are expected to align with the streamlines of the flow. In the case of a simple shearing flow, these streamlines are straight and parallel to the plates.

The test case will be an established shearing flow in which four polymers are introduced. At time $t = 0.5s$ the shear constraint is stopped and we analyse the effects.

The result of the simulation is shown in Figure 2.17. At first, the four polymers are stretched and tend to align with the streamlines. This effect is proportional to the velocity gradient of the fluid around the polymer. When the shear constraint is lifted, the polymers start to curl due to the Brownian motion. Polymers located in the top of the pipe recede due to a vortex created by sudden change in the fluid.

[3]Since we are only working with a very small amount of polymers, the effect of the polymers on the fluid will not be studied. However, these interactions will be studied in great detail in Chapter 5.

We observe that the curl action is slower than the extension as drag is more significant than the Brownian motion.

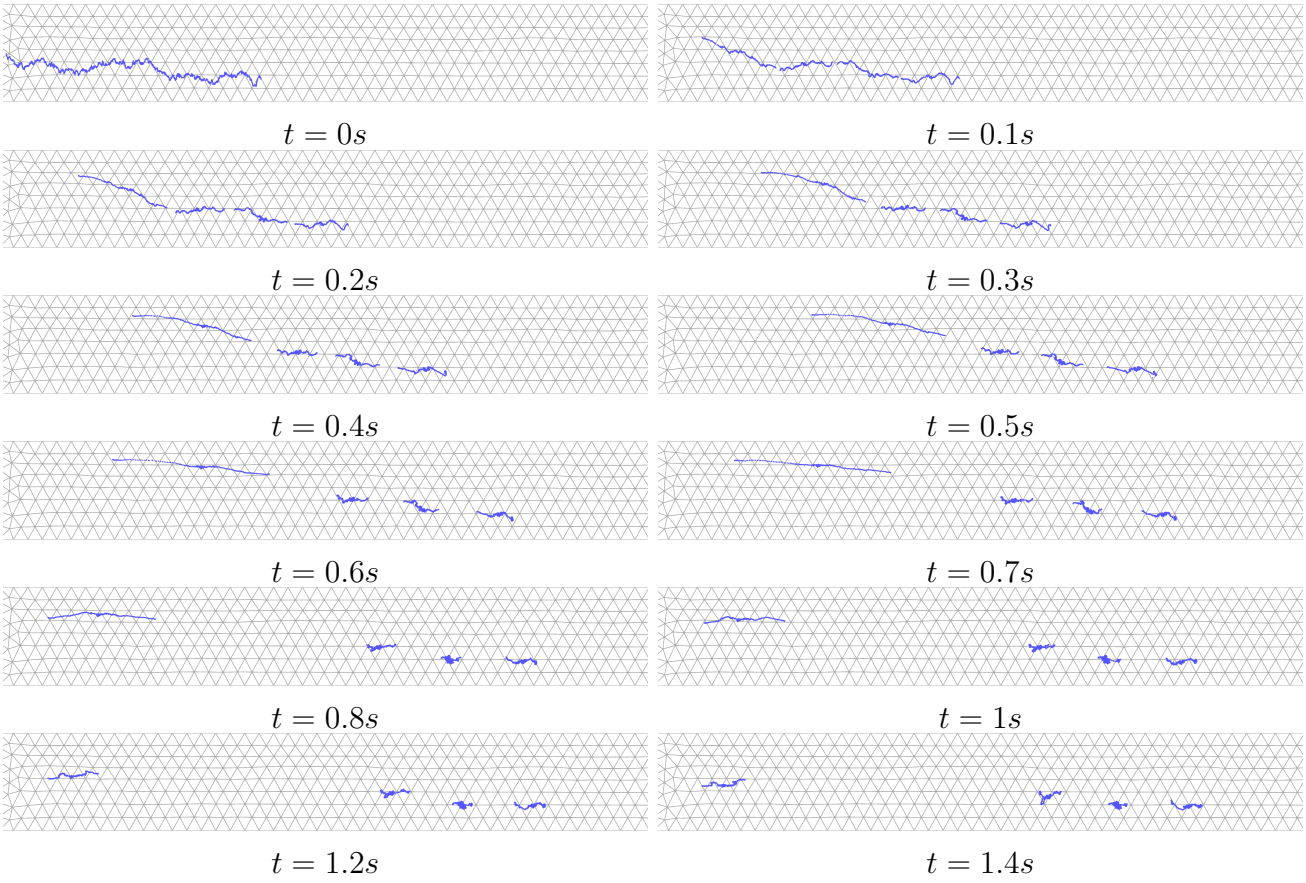

Figure 2.17: Evolution of four polymers into a shearing flow when the shear constraint stops.

Variation

Some variations of the problem can be explored. A necking or an obstacle (representing stenosis for example, see Appendix B) can be introduced into the pipe as seen in Figure 2.18. This new problem uses the same boundary conditions as in Figure 2.15, however the problem is no longer periodic as the velocity profiles aren't the same on the left and right boundaries.

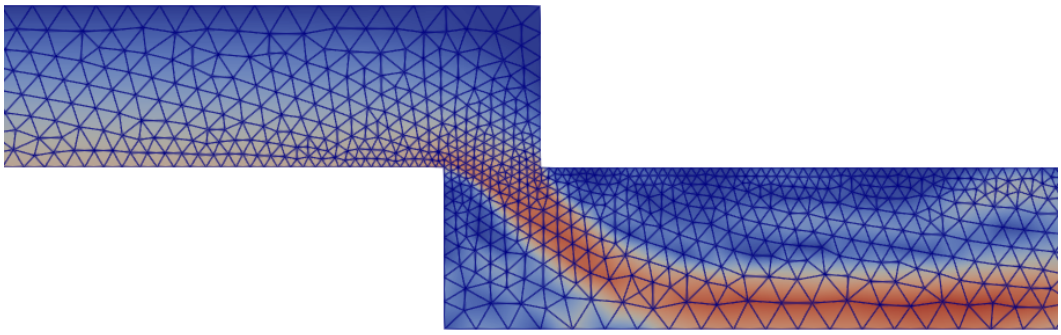

Figure 2.18: Magnitude of the velocity field at $t = 1.3s$.

It is particularly interesting to study the evolution of polymers under these new conditions as an acceleration is observed in the necking. In Figure 2.19 we can see polymers become aligned with the streamlines to pass through the necking.
This behaviour is maintained while the shear constraint dominates the Brownian motion.

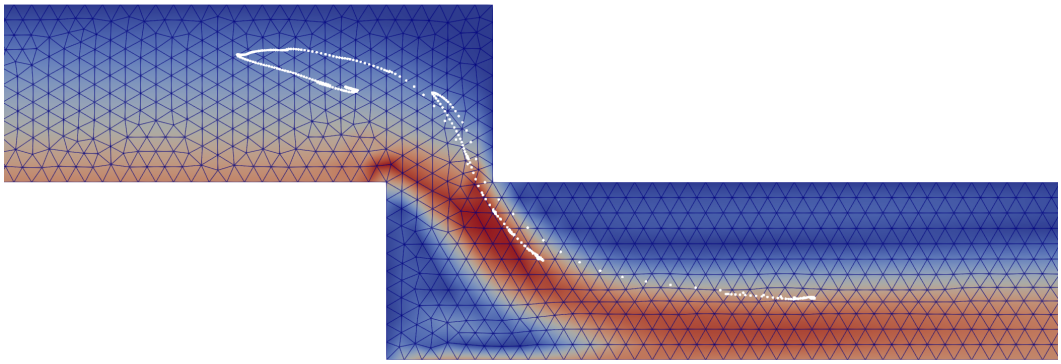

Figure 2.19: Shearing flow trough a necking with four polymer chains.

2.6 Conclusion

We have created a representation of polymer chains using a scale analogy, where every chain we simulate represents a set of microscopic polymers. This method allows us to simulate a reasonable amount of particles and observing their macroscopic behaviour.
Our elastic joints use an adapted version of the FENE model and, as a result, respect the finite extension properties. We have explored two possible structures based on an improved version of the Dumbbell model: the chain representation and the triangular representation. There are two main differences between these structures. The first is that the chain representation is more suited for larger polymers, while the triangular representation is preferable for smaller polymers. The second is that the triangular representation preserves the shape of the polymers where as the chain representation does not.

These chains allow us to use *MigFlow* to simulate non-Newtonian fluids while understanding the internal mechanisms responsible for this behaviour.

Chapter 3

Moving boundaries

Dynamic geometries or moving boundaries are the second enhancement to the *MigFlow Project*. This enables us to consider more complex domains where boundaries can move. We will consider two movements: translations and rotations. Managing these variations in geometry requires us to modify or even recalculate the mesh. The recomputed solution of the different fields is obtained using an Euler-Lagrange approach or by projecting the old mesh onto a new one.

To illustrate and develop our methods, we focus on a particular example: a magnetic stirrer (see Appendix D). These devices are widely used in laboratories all over the world making them interesting to study. For our simulations we will consider a cross section of the system as seen in Figure 3.1.

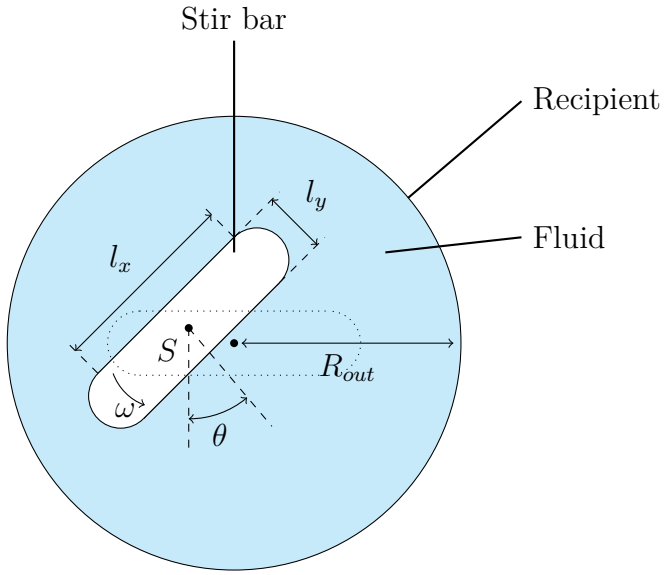

Figure 3.1: Illustration of the geometry of a stirrer.

The magnetic stir bar is a moving boundary of the fluid domain. In this chapter, we will describe the deformation of the mesh, the numerical methods used to manage these boundaries, before concluding with the results of our simulations.

3.1 Mesh deformation

When a boundary moves, the first step is to adapt the mesh accordingly. For smaller deformations, the mesh can be directly adapted without needing to re-mesh the domain. However, for larger deformation a re-mesh is necessary. Small deformations are defined as those that don't result in a poorly conditioned mesh [18] or cause triangles to intersect. In practice, a maximum displacement is considered for each node according to the size of the elements. If this value is exceeded, the mesh is fully recalculated over the domain.

We are studying two boundary movements, both will be discussed in the following sections.

3.1.1 Translational deformation

The first type of movement considered is translation. In the case of the magnetic stirrer, it corresponds to a pure translation of the stir bar as illustrated in Figure 3.2.
To move the boundary we need to adapt the whole mesh. We could have chosen to move a minimum amount of nodes but, in order to preserve the conditioning of the mesh, we have chosen to move all nodes. This minimises the maximum deformation of the elements.

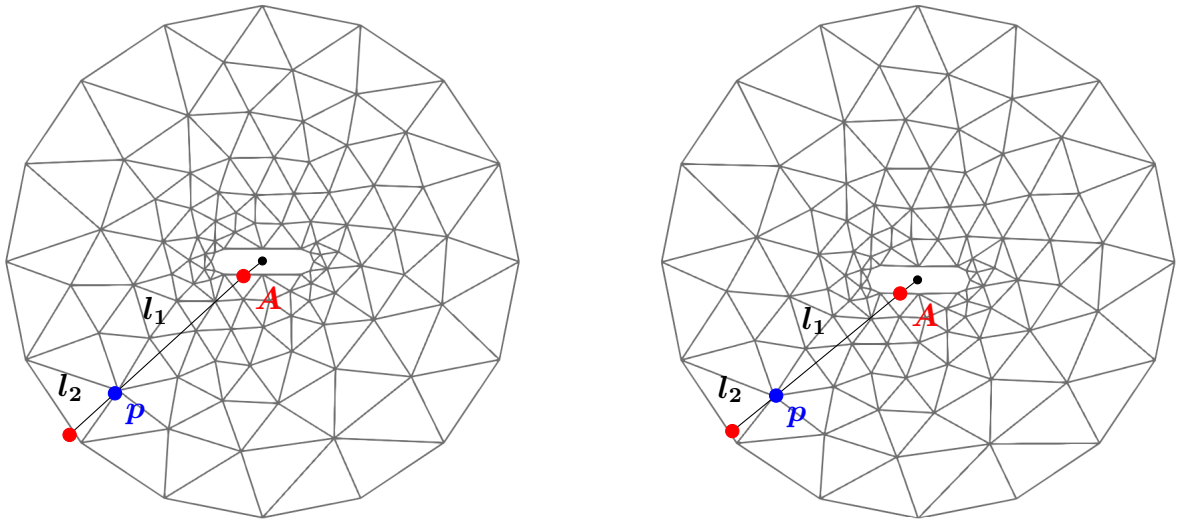

(a) Before translation of the magnetic bar (b) After translation of the magnetic bar

Figure 3.2: Deformation of the mesh during translation.

We can see that after the translation (Figure 3.2(b)), the deformation is evenly distributed over all elements, keeping the mesh as well-conditioned as possible without needing a re-mesh. Every node moves proportionally to its distance from the dynamic boundary. The corresponding mapping is described here.

$$(p'_x, p'_y) = \boldsymbol{\Delta d} \frac{l_2}{l_1 + l_2} (p_x, p_y) \qquad \forall p \in P \tag{3.1}$$

where P is the set of nodes composing the mesh, $\boldsymbol{\Delta d}$ is the displacement of the moving boundary, (p_x, p_y) is the position of a node p and (p'_x, p'_y) is its new position.

It is important to note that, in some particular cases, a translation is sufficient to reach every possible state and no rotations are required. An example of such a case is the Journal Bearing described in Chapter 4, assuming the cross section of the journal is a perfect circle.

3.1.2 Rotational deformation

In the case of the magnetic stirrer, the rotation of the stir bar must also be considered. As in the translation, the total deformation is spread over all elements. However, there are two major differences.
First, contrary to the translation, the rotation may cause a penetration between two elements, resulting in an invalid mesh. Secondly, as the points of the boundary are not subjected to the same displacement, each node has to be adapted according to its projection on the boundary.

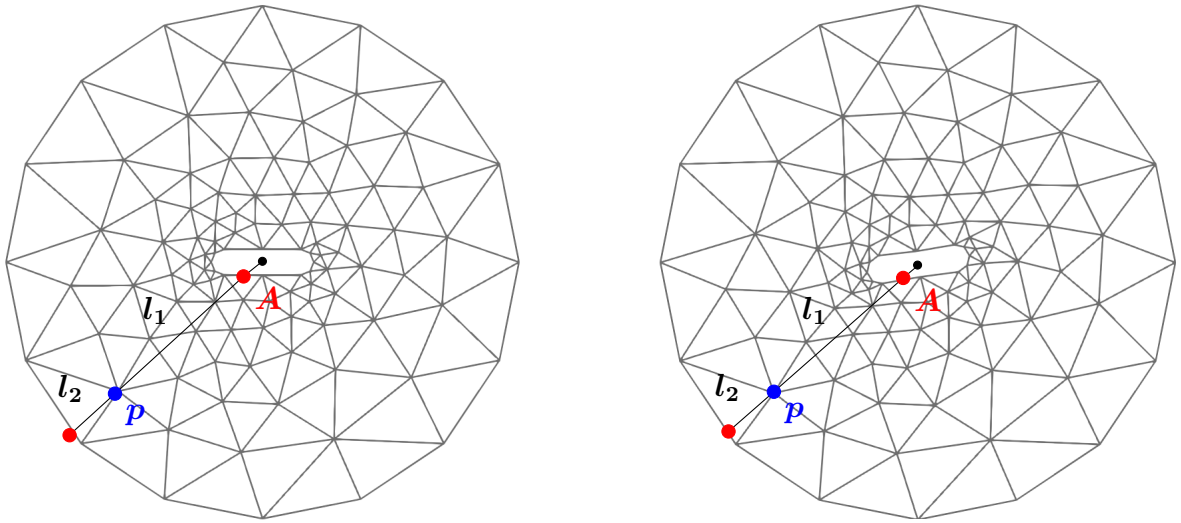

(a) Before rotation of the magnetic bar.

(b) After rotation of the magnetic bar.

Figure 3.3: Deformation of the mesh during rotation.

Figure 3.3 shows that the displacement of a node depends on point A which is its projection on the dynamic boundary. The mapping is applied to each node of the mesh and is given by the following equation:

$$(p'_x, p'_y) = \boldsymbol{\Delta d_A} \frac{l_2}{l_1 + l_2} (p_x, p_y) \qquad \forall p \in P \tag{3.2}$$

with $\boldsymbol{\Delta d_A}$ the displacement of the corresponding point A. Point A has to be recalculated for each node according to the current position and shape of the boundary at each time step. The computation of point A has a negative impact on the performance of the solver but does not modify its global complexity (which is at least $\mathcal{O}(n^2)$).

3.2 Numerical resolution

Both deformations cause a displacement of all nodes in the mesh. This displacement invalidates the Eulerian approach used to solve the fluid problem. The Eulerian approach considers a fixed mesh on which each element represents a volume element of the space. However, in the case of moving boundaries, the mesh is no longer static and an Euler-Lagrange approach must be considered [19].

The mesh needs to be re-calculated if the deformation is too large or if a rotation causes elements to penetrate. In such cases, we need to project the previous solution of the fields on the new mesh. In practice, *MigFlow* stores the mesh in an OCTree (see Appendix C), a structure that enables us to retrieve the element of each new node with a time complexity of $\mathcal{O}(\log N)$. The pressure and velocity fields at each new node are computed using the shape functions associated with the corresponding element before recalculating the porosity.

Projecting a solution on the new mesh has thus a complexity of $\mathcal{O}(N \log N)$ where N is the number of nodes. The worst-case complexity of a complete re-meshing is lower than $\mathcal{O}(N^2)$ for *GMSH* (which is the mesh generator used [18]).
These two complexities are lower than the overall complexity of *MigFlow* and therefore, the projection and re-mesh do not impact the time complexity.

3.3 Application

We can use this method of managing dynamic boundaries to study the magnetic stirrer.

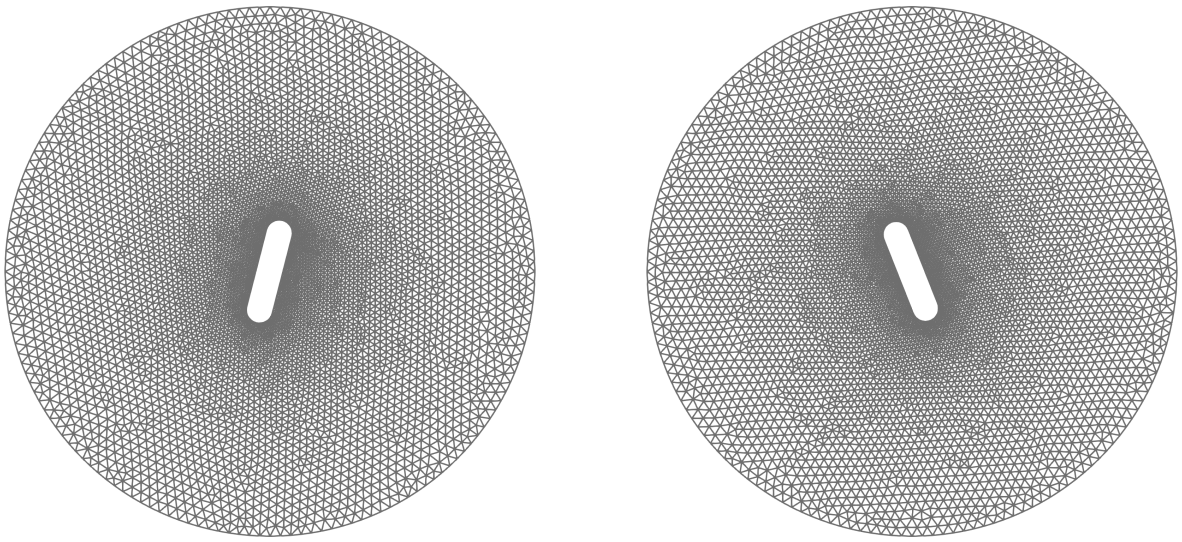

Figure 3.4: Mesh of the stirrer undergoing a re-meshing and a projection over a single iteration.

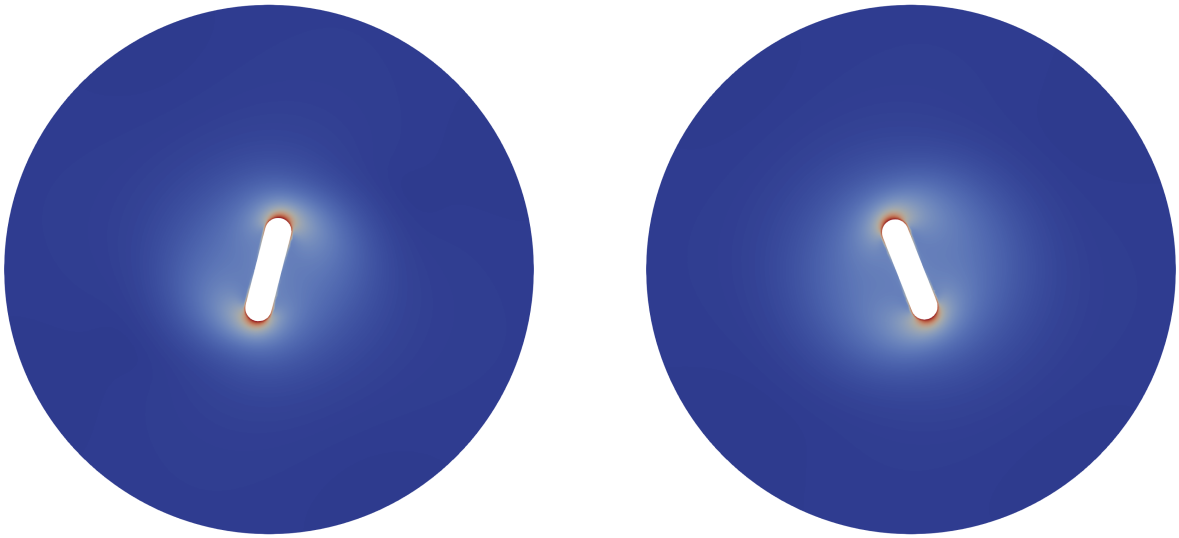

Figure 3.5: Velocity field of the stirrer undergoing a re-meshing and a projection over a single iteration.

Figures 3.4 and 3.5 show the results of the previous example. In this test case, a constant torque is applied on the magnetic bar (induced by an electromagnet).

The objective of the magnetic stirrer is to mix a solution. As such, we can study the impact of the geometry of the stir bar on its mixing efficiency. Firstly, we will consider a stir bar with a *stadium shape* as in Figure 3.1. Secondly, we will consider one that is *circular*, resembling the journal bearing assembly[1]. A two-phase fluid fills the clearance space between components. The concentration of each fluid is defined respectively as: $\{C_1, C_2\}$. Initially, the phases are separated on either side of the domain (see Figure 3.6). The same torque is applied to each stirrer and the variance of the concentration of $\sigma^2_{sys}(C_1)$ over the whole domain is monitored. The result is shown in Figure 3.7.

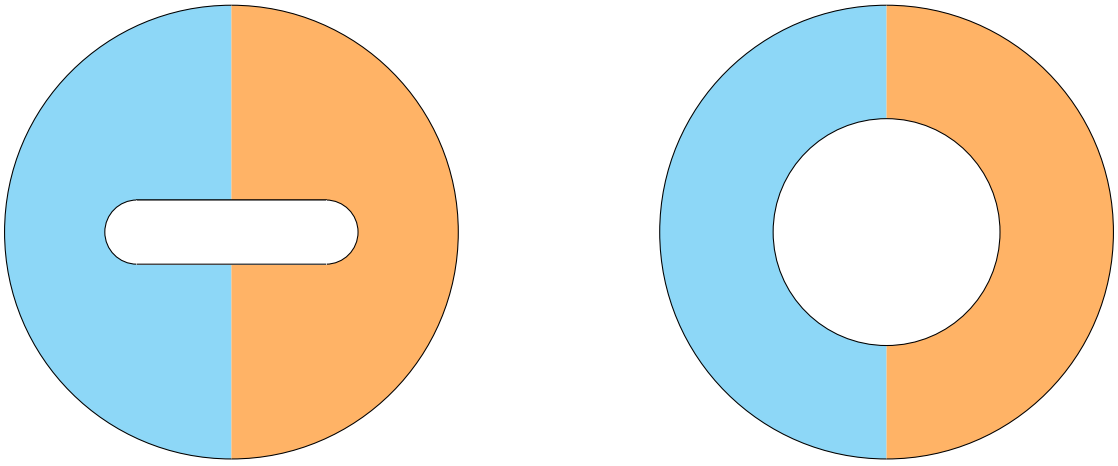

Figure 3.6: Illustration of two stirrers (left - stadium (bar) stirrer, right - circular stirrer) with a two-phase fluid (each colour represent a phase) at the initialisation.

[1]This geometry has been chosen for the sake of simplicity as it is thoroughly studied in the next chapter and provides excellent contrast with the standard stir bar.

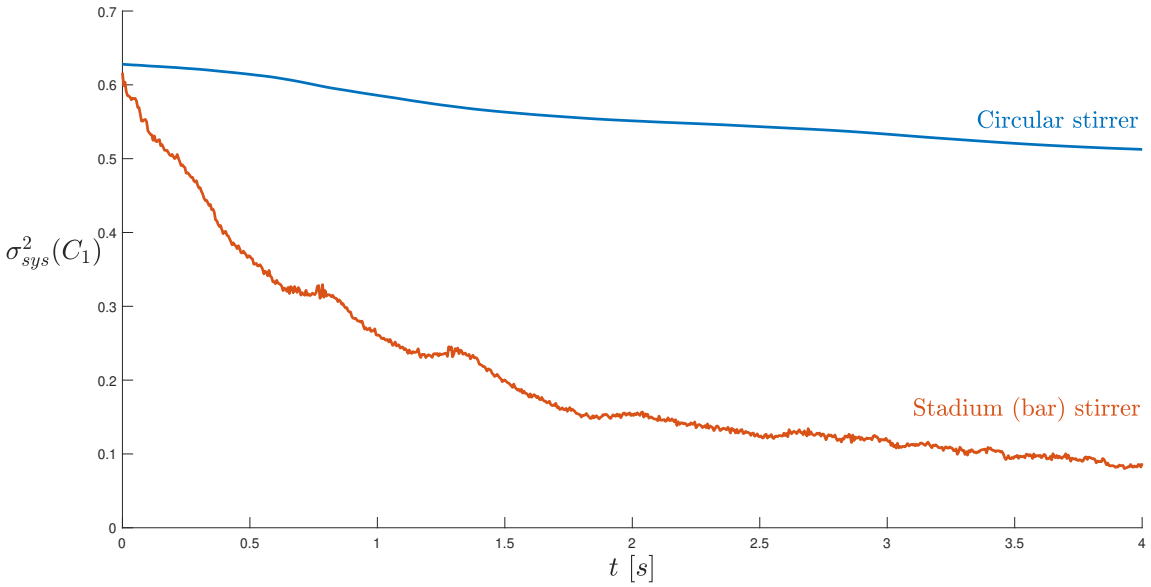

Figure 3.7: Comparison of the mixing capability of the two stirrer.

We see that the variance of concentration of the *stadium stirrer* diminishes quicker than that of the *circular stirrer*. This means the domain homogenises faster and therefore the device is more efficient.

Note: the measurement of the variance of concentration is not used in practice since it is impossible to know its exact value at every given time step [20]. However, it gives an adequate indication of the uniformity of the solution and is perfectly usable in the context of numerical simulations.

Polymers may be added to the fluid and the results of these simulations are given in Figure 3.8. The mesh evolves over time and the polymers elongate and curl as the stir bar mixes the solution (a more detailed figure can be found in Appendix E).
This confirms our implementation of the moving boundaries and the compatibility with the *MigFlow* particles as well as our polymers. Additionally, the maximum extension of polymers is preserved due to the adapted FENE model (see Chapter 2).

3.4 Conclusion

We have developed a method to handle moving boundaries in *MigFlow* that is applicable to 2D finite element problems in general. This allows us to simulate more complex systems in which the domain evolves over time or contains moving parts.
These moving boundaries can be applied to many problems, including the magnetic stirrer, the journal bearing and the delayed die swell (the last two will be discussed in the next chapters).

The following chapters aim to check the validity of our polymers and our dynamic boundaries by comparing simulations to experimental results.

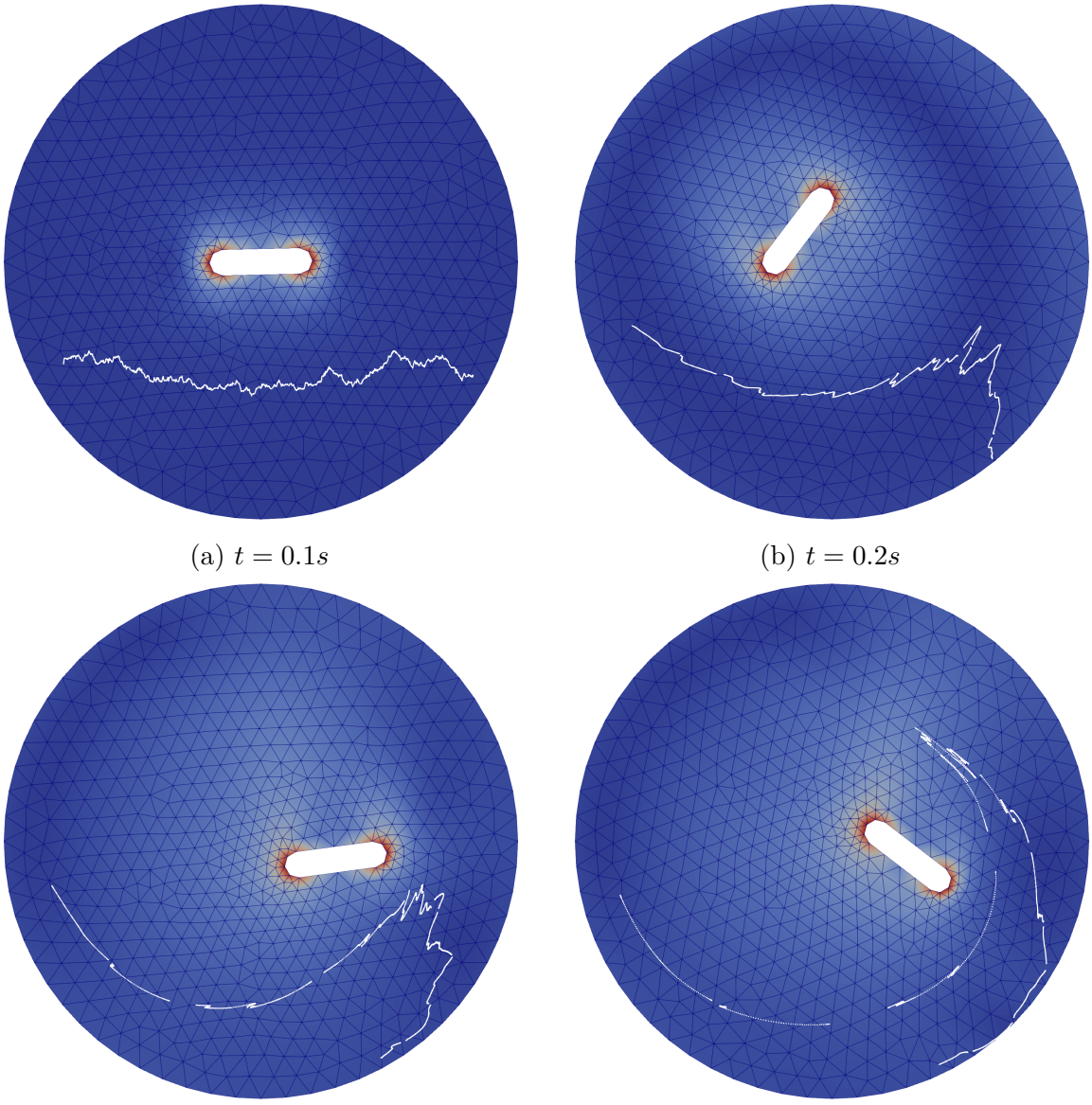

(a) $t = 0.1s$ (b) $t = 0.2s$

(c) $t = 0.3s$ (d) $t = 0.4s$

Figure 3.8: Simulation of a magnetic stirrer with polymers.

Chapter 4

Journal Bearing

The study of flows between eccentric cylinders has many applications in engineering such as rheology, industry etc. In this document, we will consider a two-dimensional laminar flow between two eccentric cylinders. Within our model, all fluids are considered to be incompressible. We will assume the geometry of both cylinders to be perfect and their longitudinal axis to be parallel at all times. Thermal effects and flows along the longitudinal axis are not considered for this application.

Based on the hypothesis described above, we have chosen to focus on the specific application of *journal bearings* for the remainder of this chapter.

Bearings are one of the most common and important components in machines as they transfer loads, prevent undesirable motion and support rotating components e.g. shafts. In traditional bearings, relative motion between elements leads to wear, friction losses and a decrease in overall efficiency.

Journal bearings aim to minimise these losses further by using fluid films to reduce contact between rotating and stationary components. This makes journal bearings ideal for machines rotating at high speeds such as compressors [21], turbines [22], train engines [23] etc.

In this chapter, we will develop a simulation of the journal bearing assembly using the tools we have previously implemented: immersed polymers and moving boundaries. The polymers allow us to simulate non-Newtonian fluids. The moving boundary allows us to represent the moving shaft. We start by reviewing the current state of the art and the physics behind journal bearings. Our model for Newtonian fluids will then be validated by comparing our results to scientific papers. A parametric study is followed by a study of stability. Adding polymers allows us to compare Newtonian and non-Newtonian lubricants.

4.1 State of the art

The physics of journal bearings is well-documented due to its many applications and high efficiency. In the early 20th century, Sommerfeld [24] and Harrison [25] developed independent solutions to the infinite length journal.

Sommerfeld, being the first to have developed such a model, gave his name to the non-dimensional number Λ (also noted S depending on the source). This number, referred to as the *bearing number* or *Sommerfeld number* (Equation 4.1), depends on the characteristics of the fluid and the specific geometry of the bearing. We will use this value multiple times during this chapter.

$$\Lambda = \frac{2\pi \cdot \mu \cdot \omega}{c^2} \tag{4.1}$$

where μ is the viscosity, ω is the rotational velocity and c is the clearance.

Further notable studies were carried out when Christopherson [26], Raimondi and Boyd [27] presented solutions for the finite journal bearing based on Reynolds' equations.

A decade later, Raimondi [28] created a numerical solution for the gas lubricated journal bearing of finite length. This research is pertinent in areas where low drag, high rotation and long life are necessary or when liquid lubrication is not an option.

The study of cavitations in the journal bearing is a vital topic as they may result in disastrous consequences. When the pressure in the fluid drops under the specific vapour pressure, gaseous pockets are created. These pockets collapse when the pressure increases again. The resulting shock waves may cause severe damage to the assembly. Heller [29] was the first to have presented a numerical solution using Reynolds' equations. A numerical solution was then studied by others including Aitken [30] and Heshmat [31] in different contexts and with different hypotheses. The evolution of technology has allowed for more precise detection and predictions such as those shown by Poddar [32].

As the power of computers grew, so did the available numerical tools. The first numerical models were implemented in the late 1950s by Hays [33] using an IBM 650 digital computer that took 15 minutes to compute each solution.

The development of computational fluid dynamics (CFD) paved the way for a new approach. Models such as FLUENT [34] and OpenFOAM [35] were used, for example, by Piekos [36], Gertzos, Nikolakopoulos and Papadopoulos [37] to simulate the journal bearing. This made multiphase flow analysis and the study of cavitations more reliable.

The study of journal bearings was not limited to Newtonian fluids. Since the late 1950s, research such as the *impact of oil lubricants* by Gecim [38] and *polymer-thickened lubricants* by Beris [39] have examined the impact of non-Newtonian lubricants on the performance of journal bearings. Others like Okrent [40] chose to focus on the effect of viscosity on the wear of the shaft.

Studies concerning non-circular geometries and compressible fluids have also been published by, among others, Raimondi [27] and Piekos [36] but this is outside the scope of this project.

4.2 Physics of the journal bearing

Before presenting the model we created using *MigFlow*, it is important to understand the underlying physics of the journal bearing.

4.2.1 Geometry

The journal bearing is comprised of two main parts: a fixed outer bearing of radius R_{out} and an inner rotating journal with a radius of R_{in}. In this document, the non-dimensional notation $r = \frac{R_{in}}{R_{out}}$ is used to define the radius of the journal proportionally to the bearing radius. The clearance space between these two cylindrical components, noted c, is filled with a lubricant that is carefully chosen based on the intended application. A fluid with a high viscosity is generally preferred at low speed and high loads while a low viscosity fluid is used at high speed and low loads. The rotational speed and the load of the journal are respectively ω and W.

Furthermore, the eccentricity e is defined as the offset of the centre of the journal with respect to the centre of the bearing. The minimum film thickness is noted h. The attitude angle ϕ is characterised by the angle between the load and the line joining both centres (please see figure 4.1).

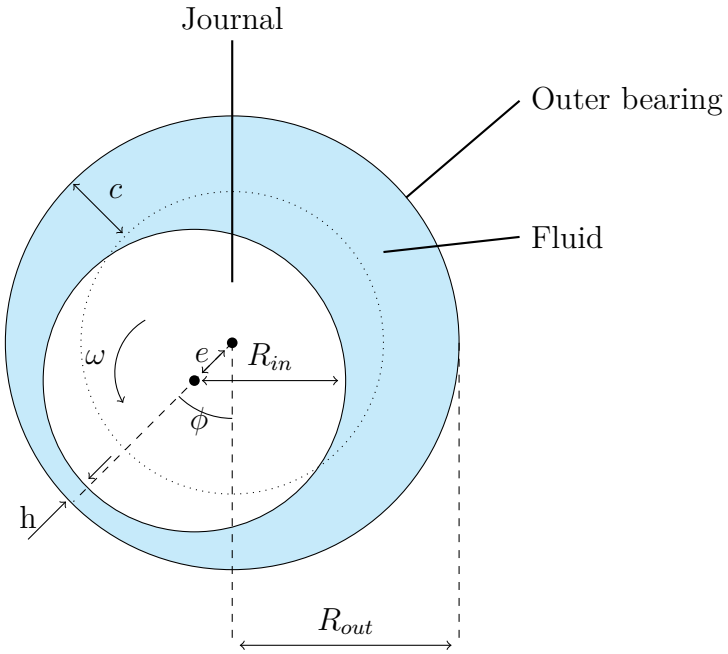

Figure 4.1: Illustration of the geometry of the journal bearing.

4.2.2 Working principle

The simple design of the journal bearing means the assembly is highly dependent on both the geometry and the characteristics of the lubricant. The bearing is inclined to become unstable at high rotating speeds and when $r \to 1$. In such cases, the journal comes into contact with the outer bearing and revolves around this boundary. Further stability studies will be carried out in a following section.

Figure 4.2 illustrates the working principle of the assembly.

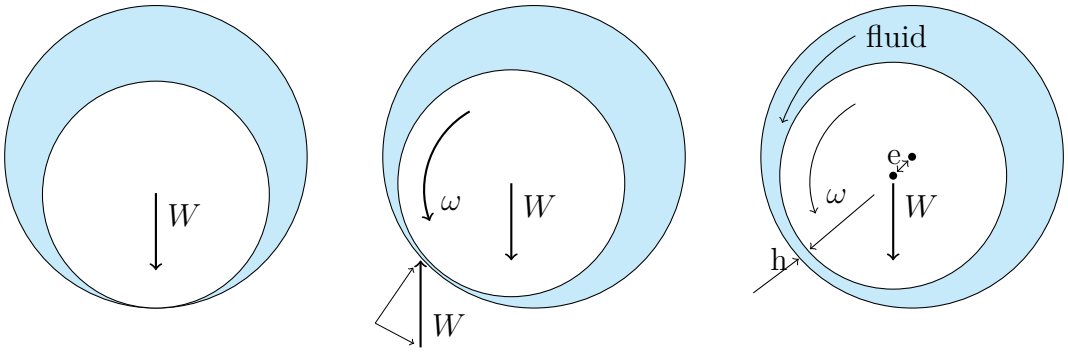

Figure 4.2: Working principle.

While stationary, the journal sits on the outer bearing.
The journal then begins to rotate and the fluid is pulled between the metal components creating a Couette flow [17] (see Figure 4.3). To preserve conservation of mass, a region of high pressure and a region of low pressure appear in the fluid, provoking a pressure gradient in the channel. A Couette-Poiseuille flow is generated and this, in turn, modifies the resulting force applied to the journal. The rotating journal is lifted as a thin film of lubricant inserts itself between the cylinders.

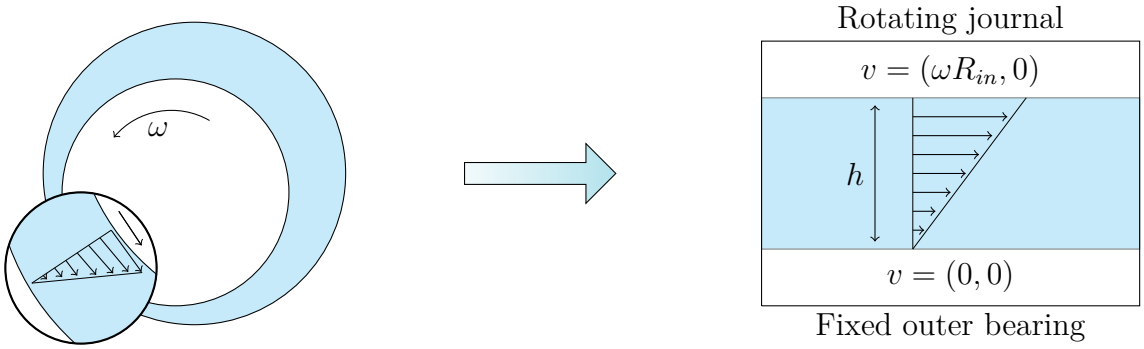

Figure 4.3: Couette flow in the journal bearing.

The load-carrying properties of the bearing assembly are dependent on the pressure around the circumference of the journal.
At the start, the pressure distribution is constant and we have $\frac{\Delta p}{p_0} = 0$. As the bearing begins to move, the misalignment causes asymmetry throughout the assembly. The fluid channel separating the two components decreases as the eccentricity grows. Where the fluid film becomes thinner, the pressure increases. The maximum is reached just before minimum thickness after which the pressure drops suddenly (see Figure 4.4).

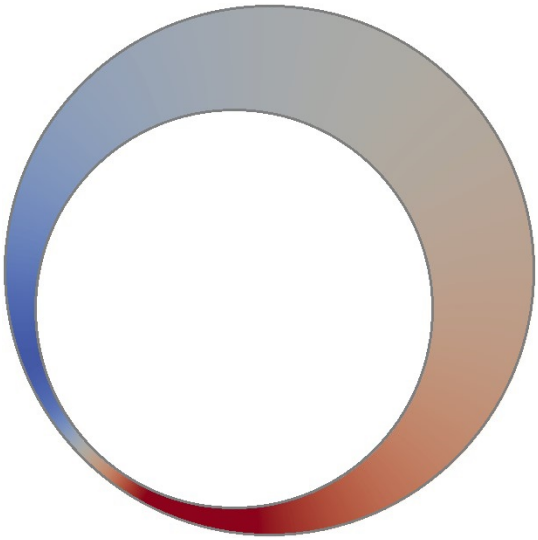

(a) Screenshot of a simulation. Red zones indicate high pressure regions while blue indicate low pressure regions.

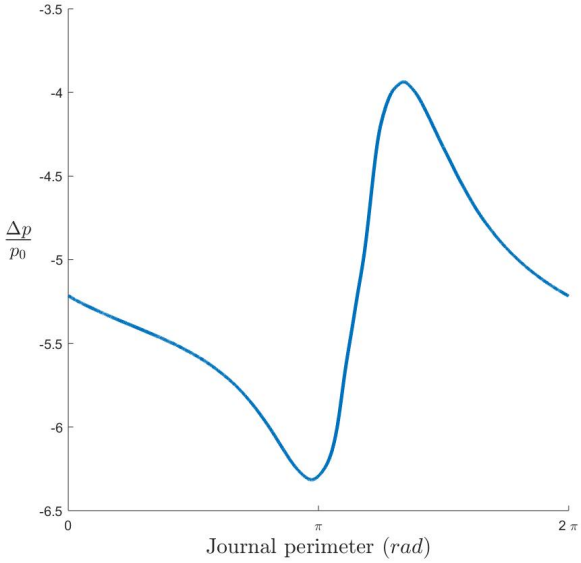

(b) Qualitative results.

Figure 4.4: Example of steady state pressure distribution around the perimeter of the journal.

4.3 Validation

The journal bearing simulation we've developed combines moving boundaries and immersed polymers. An example of a mesh that we used may be seen in Figure 4.5. This first step is to consider lubricants that are Newtonian fluids. The polymer deformation to simulate the non-Newtonian behaviours will be studied in a subsequent section of this chapter.

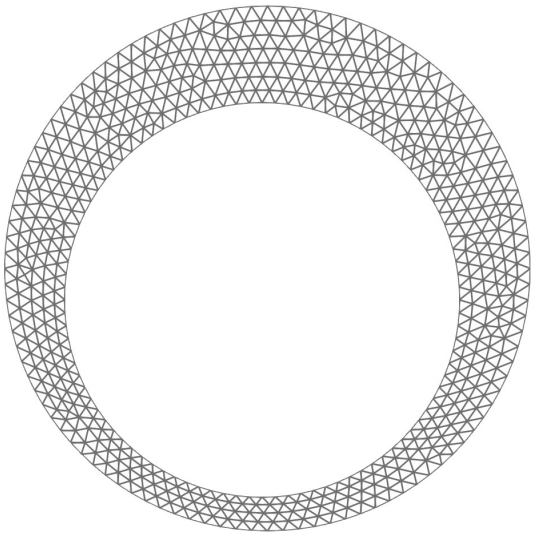

Figure 4.5: Example of a mesh used after several iterations (see Chapter 3).

This model is validated by comparing our results to available numerical data [41]. We proceeded iteratively to achieve the first two figures. We modify two non-dimensional parameters, the loading parameters and the Sommerfeld number, until the desired *steady state* eccentricity is reached (see Figures 4.6 and 4.7).

The loading parameter and the Sommerfeld number are defined respectively as:

$$\zeta = \frac{m \cdot g}{2 \cdot r \cdot P_a} \quad \text{and} \quad \Lambda = \frac{2\pi \cdot \mu \cdot \omega}{c^2}$$

As a reminder, we are using non-dimensional notations to prevent any loss of generality.

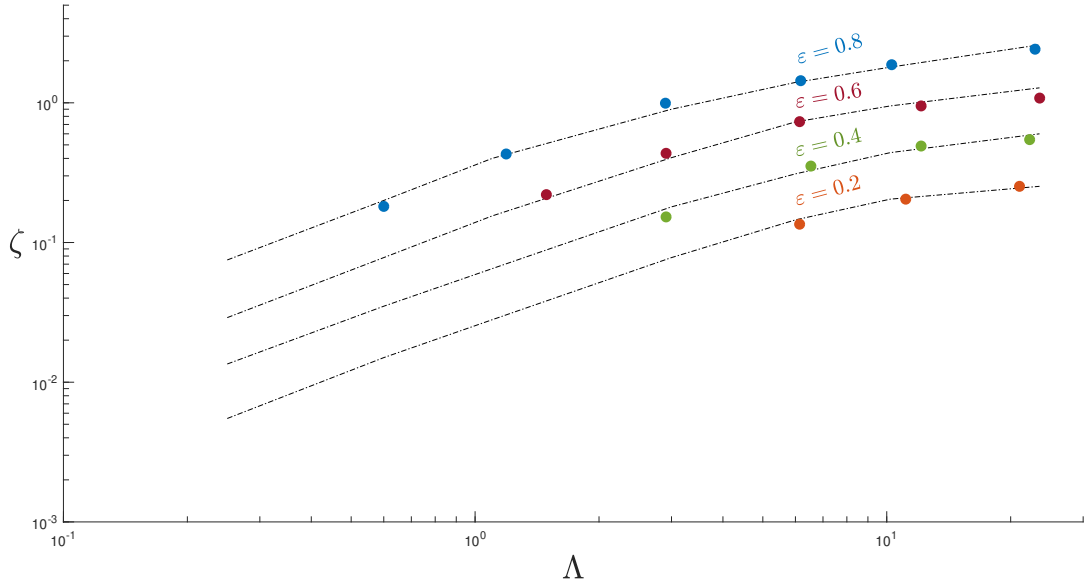

Figure 4.6: Comparison of the evolution of the load parameter with respect to the *Sommerfeld number* for different eccentricity ratios $\varepsilon = \frac{e}{c}$. Our results are shown in *colour* while those of Piekos and Raimondi are represented by *dotted and dashed* lines.

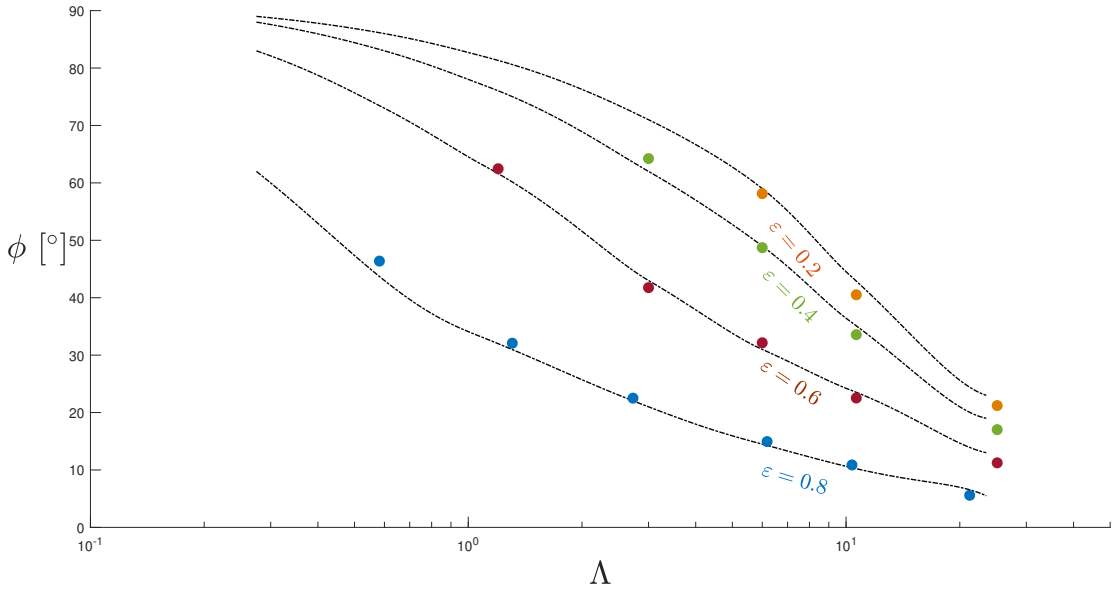

Figure 4.7: Comparison of the evolution of the attitude angle with respect to the *Sommerfeld number* for different eccentricity ratios $\varepsilon = \frac{e}{c}$. Our results are shown in *colour* while those of Piekos and Raimondi are represented by *dotted and dashed* lines.

As for pressure distribution, Figure 4.8 shows that our results follow similar trends to those of Stanley [41].

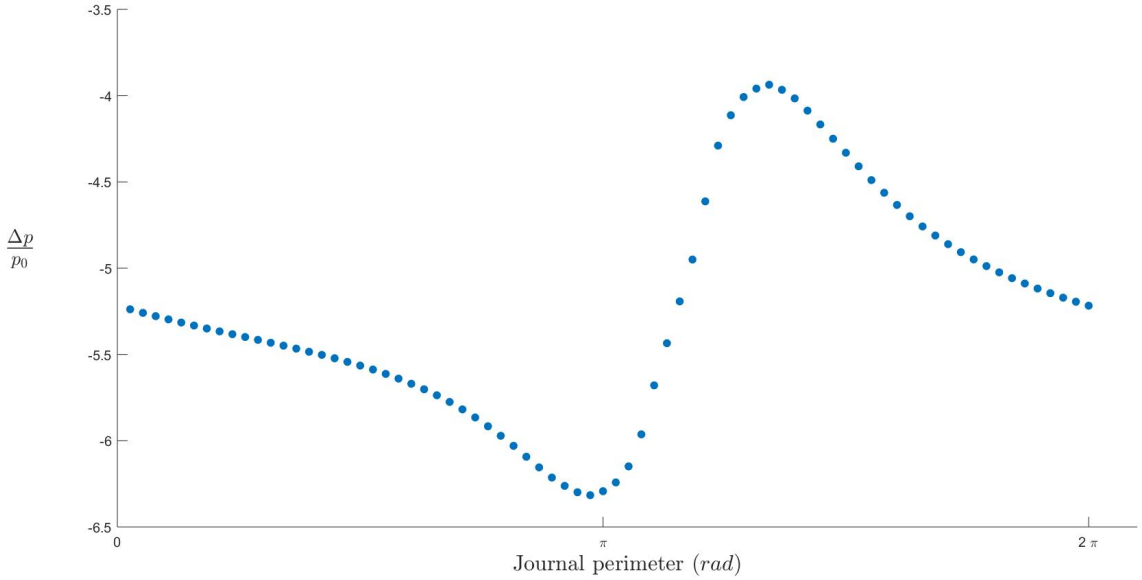

Figure 4.8: Example of steady state pressure distribution around the perimeter of the journal.

Our simulations tend to become unstable at low Sommerfeld numbers and load parameters making it difficult to obtain these low-range values. Despite this, all of these results correlate with those of Piekos and Raimondi [41]. We may thus assume that our simulations are valid. The next sections are dedicated to a parametric study, a stability study and simulations of the system with non-Newtonian fluid. These studies enable us to explore the capabilities of our model and the mechanisms at the origin of these non-Newtonian behaviours.

4.4 Parametric study

As stated previously, the journal bearing has a strong tendency to become unstable in certain conditions. As a result, it is vital to identify the parameters that have a significant impact on stability. With this in mind, we have studied the influence of the fluid density ρ and viscosity ν, the non-dimensional radius of the journal r, the load W applied to the journal and the rotational velocity ω of the journal.

Both the journal radius r and the velocity ω have a particularly significant impact on the overall stability of the system and will be discussed in further detail.
Figure 4.9 shows the time evolution of the attitude angle for different values of ω with a constant journal radius.

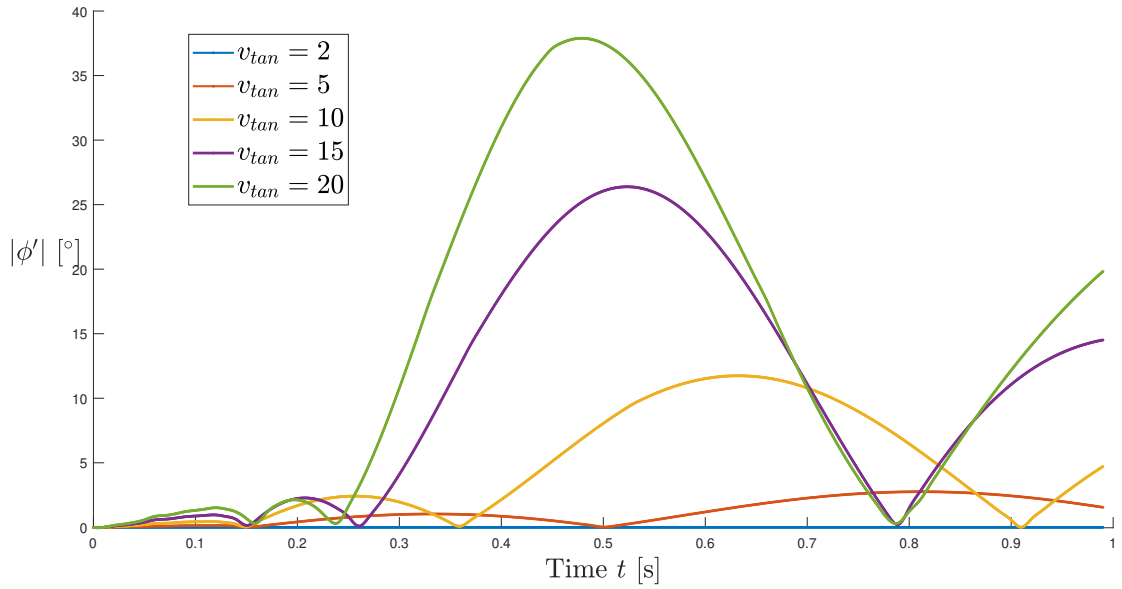

Figure 4.9: Evolution of the absolute value of the attitude angle for different values of the tangential velocity of the journal $v_{tan} = r \cdot \omega \quad [s^{-1}]$.

At first, the bearing is very stable. As the tangential velocity increases, it causes a behavioural change and an oscillatory response occurs. Both the amplitude of the attitude angle and the frequency of these irregular oscillations increases with ω. Eventually, the journal is completely unstable and rotates around the perimeter of the bearing.

Figure 4.10 shows the evolution of the attitude angle for different values of journal radius r and a constant velocity.

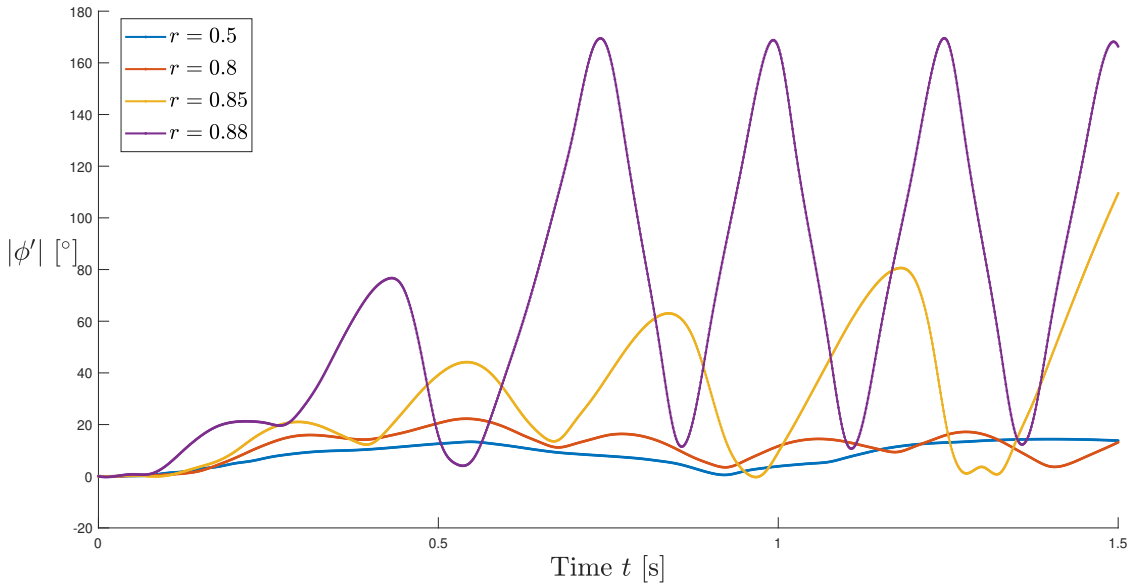

Figure 4.10: Evolution of the absolute value of the attitude angle for different values of journal radius r.

It is clear that the assembly becomes unstable as the radius of the journal increases. Note that for these two figures we are working with the absolute value of the attitude angle which is limited to the interval $|\phi'| \in [0°, 180°]$. As a result, though the purple line may look stable, it is in fact unstable and rotating around the outer bearing.
This section aims to highlight the variables prone to causing unstable conditions. We have shown that the assembly is particularly sensitive to the geometry, more specifically to the radius ratio r. This emphasises the importance of choosing the appropriate radius for the desired application.

4.5 Stability study

Now that some of the physical parameters of the journal have been explored, we use these results to analyse its stability and its response to perturbations with parameters leading to a stable state. An example can be seen in Figure 4.11.

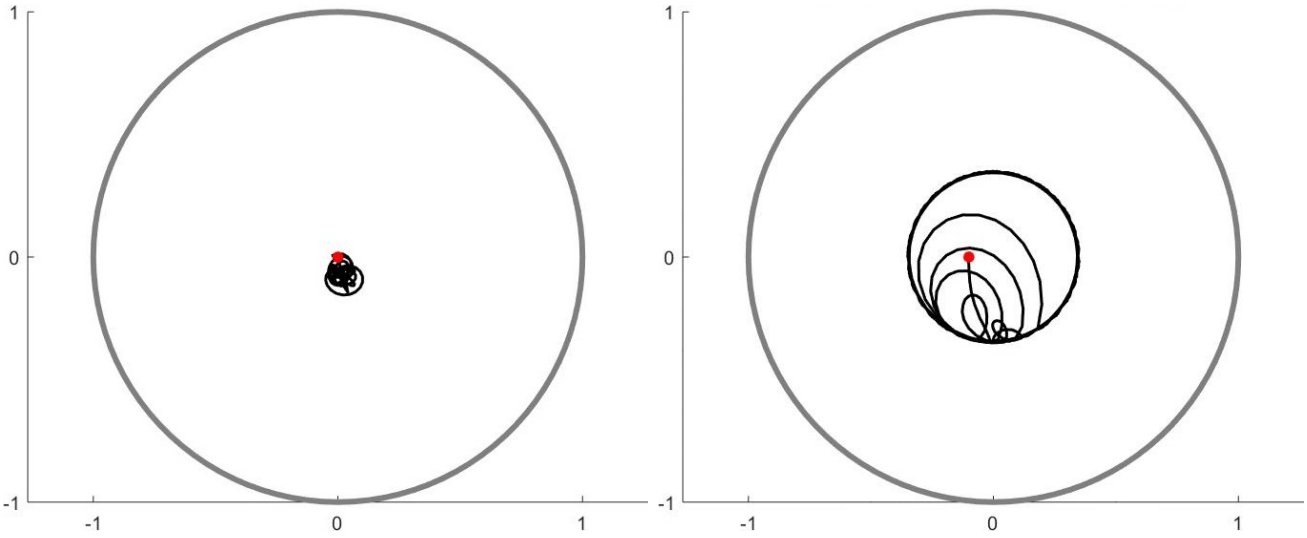

(a) Example of a stable journal.

(b) Example of an unstable journal.

Figure 4.11: Example of stable and unstable conditions.

A load is considered on the journal and two perturbations are performed: a change of the angular velocity ω and an impulse on the journal. Both perturbations have practical applications in the industry where the journal bearing is used to maintain rotating shafts with minimum friction. We see that the rotational velocity may vary over the course of its use or a sudden impulse may be applied to the shaft and influence the journal.

Note that a stable journal tends to settle at a given attitude angle according to the set of parameters used. We observe the evolution of this attitude angle over time for the different perturbations in Figure 4.12, 4.13 and 4.14.

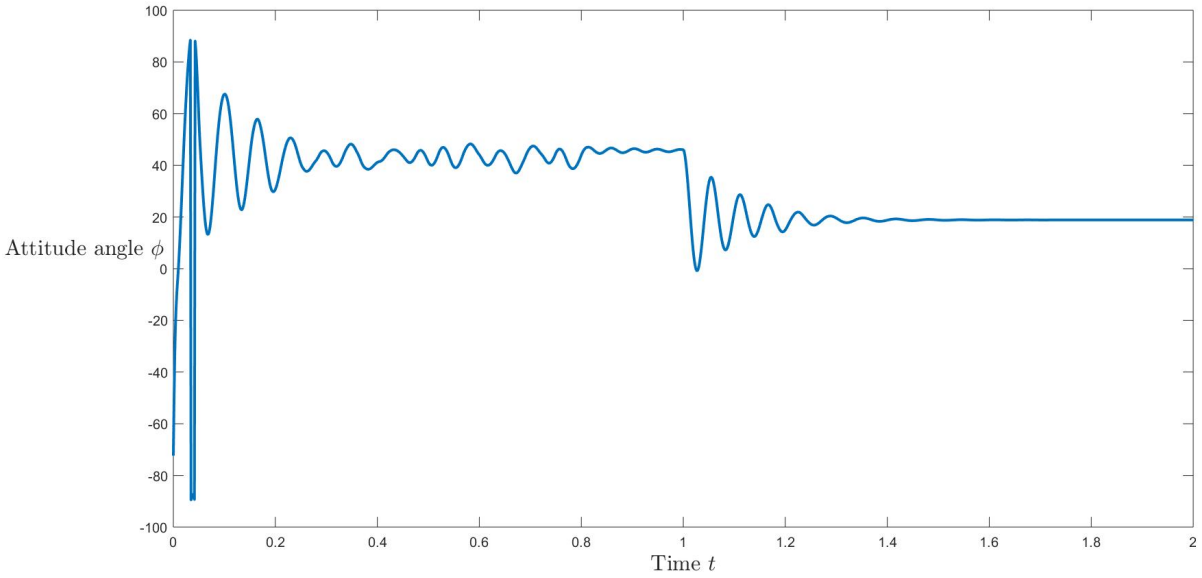

Figure 4.12: Journal's response when its angular velocity is halved (i.e. $\omega' = \frac{\omega}{2}$) at time $t = 1$.

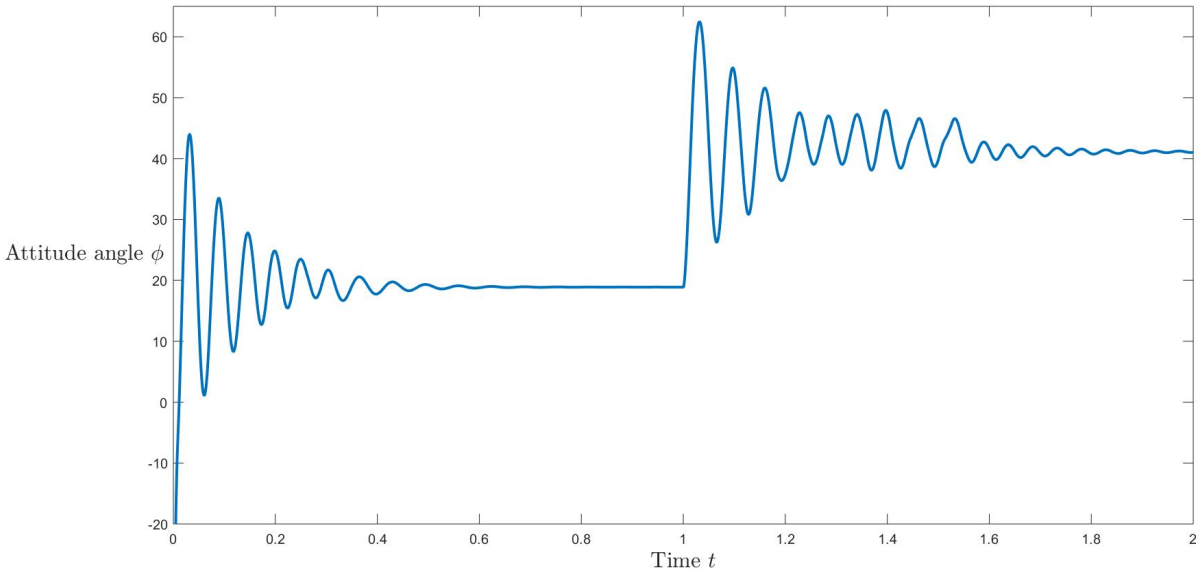

Figure 4.13: Journal's response when its angular velocity is doubled (i.e. $\omega' = 2\omega$) at time $t = 1$.

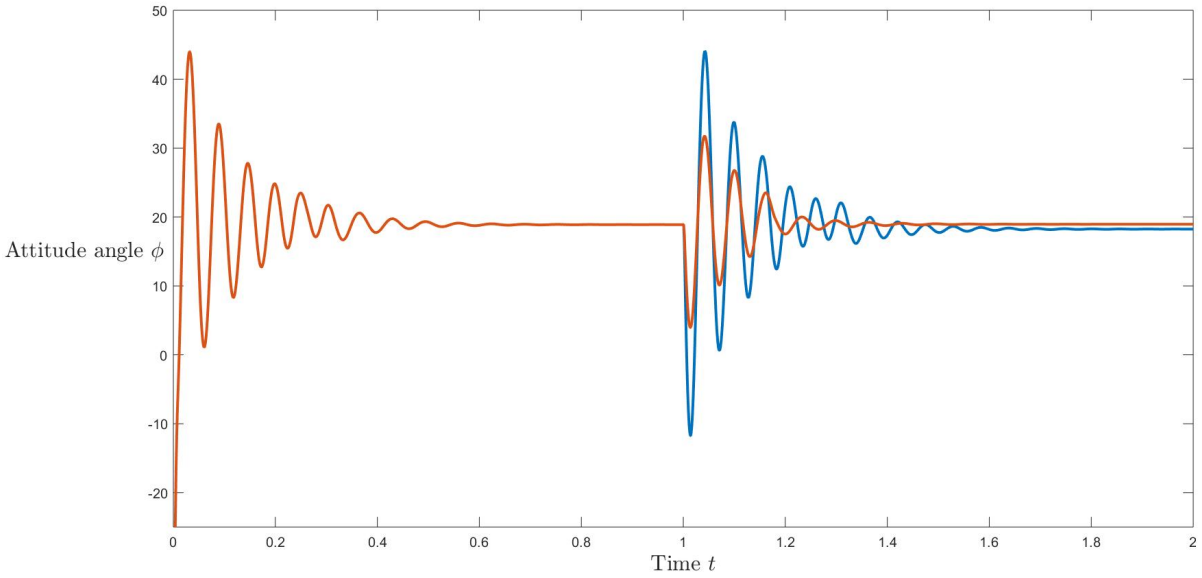

Figure 4.14: Journal's response to a impulse at time $t = 1$. Orange: horizontal perturbation of the same magnitude as its weight. Blue: horizontal perturbation of twice its weight.

We see that the response of the journal is instantaneous. For all cases, the system responds directly with an overshoot and then oscillates until reaching a new stable state. For smaller velocities or perturbations, the oscillations are smaller and the system stabilises faster.

4.6 Polymer deformation

By adding polymers to the system, the lubricant becomes non-Newtonian and the properties of the fluid change. Therefore, we expect the properties of the journal bearing assembly to also change.

As stated previously, a stable journal will settle at a given attitude depending on the parameters that are used, namely the load.
Figure 4.15 shows that, regardless of fluid used (Newtonian or non-Newtonian), this attitude angle follows a linear relationship with the normalised load. This is an important result as it states that the attitude of a stable journal is not impacted by non-Newtonian properties.

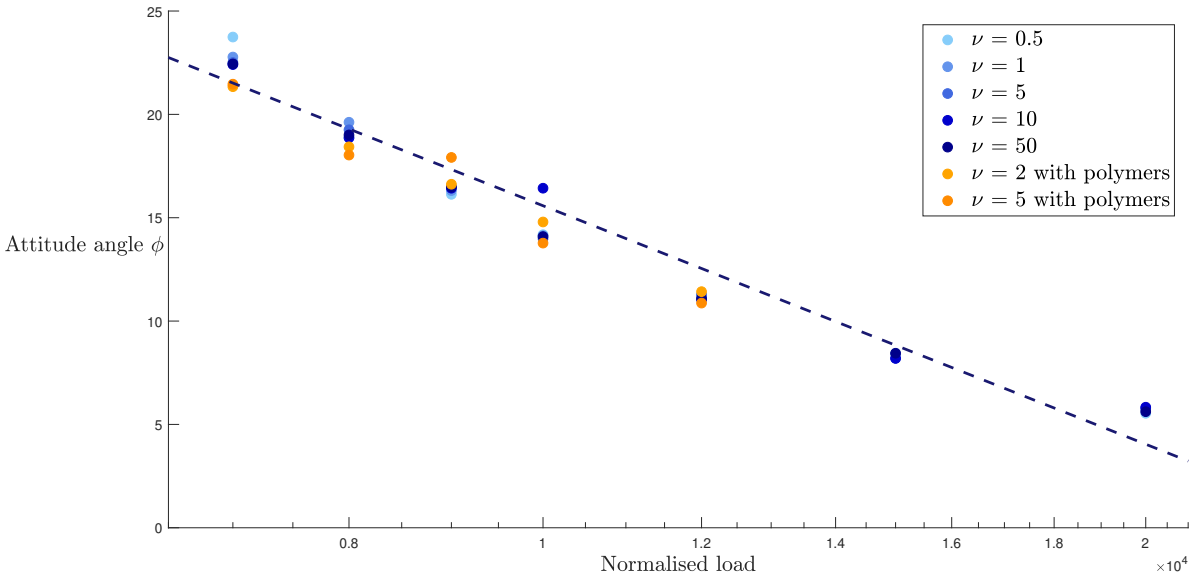

Figure 4.15: Evolution of the attitude angle according to the normalised load for different fluids. The dashed line is a linear regression of the data points from our experiment.

From the results of our numerical experiment, we observe a correlation coefficient of 92.4%, which is high enough to lead us to confirm the linear relation. This is in agreement with the work of Berker [42] in which he conducted a similar experiment. The slope of his linear regression is 0.168 while we obtained a slope of 0.16. Since Berker's results were experimental, we are confident in the validity of our results in general.
These results also seem to be compatible with the hypothesis made by Berker that the Sommerfeld number Λ is correlated to the attitude angle and the fluid film thickness.

We can now analyse the evolution of the position of the journal in the bearing and how it is impacted by non-Newtonian behaviour. With the purpose of doing so, we apply a periodic load and observe the evolution of the eccentricity of the journal over time for Newtonian and non-Newtonian lubricants. Figure 4.16 shows the results of this over a single period. Though the results of both fluids seem similar, the difference becomes apparent when we take a closer look. We observe that the journal immersed in a non-Newtonian fluid tends to remain at maximum eccentricity for a longer time. Rastogi and Gupta [43] conducted a similar experiment with the same conclusion. We deduce that, for a more viscous fluid, the presence of an elastic behaviour reduces the thickness of the fluid film.

From a practical standpoint, if this fluid film is insufficiently thick, non-Newtonian lubricants may lead to higher erosion, general loss of performance and reduce the lifespan of the bearing. On the other hand, if the periodic load is heavier or if the period is shorter, then non-Newtonian behaviours will maintain the journal in a steady position for longer.

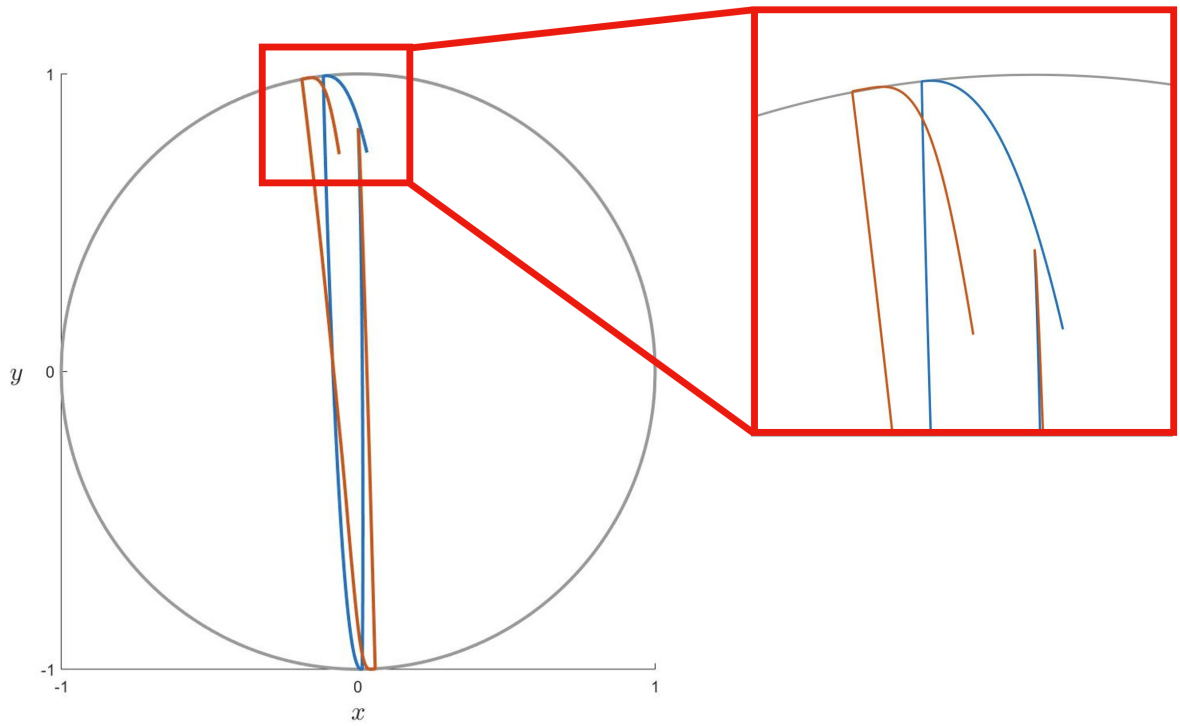

Figure 4.16: Evolution of the locus of the eccentricity ratio of a journal subjected to a periodic load. The blue line corresponds to the Newtonian case and the orange line corresponds to the non-Newtonian case.

4.7 Results

In this section, we focus on some of our additional simulations.

In the following figure, we track the evolution of two bearings: one with polymers immersed in the fluid and one without (while maintaining a constant viscosity and density).
Examples of such simulations are shown in Figure 4.18 and Appendices F and G. Note that the polymers are generated in a straight line to better observe their influence on the system and vice-versa.

Both bearings behave differently. The journal bearing that uses a Newtonian fluid as a lubricant tends to respond faster to the periodic load. In the case of the journal bearing that uses a non-Newtonian lubricant, some polymers elongate under the influence of the journal while others slowly contract due to the Brownian motion.
The ability to simulate a journal bearing with polymers is very interesting for many industrial applications. We know that a non-Newtonian fluid is, for example, better suited for more violent variations of the load.

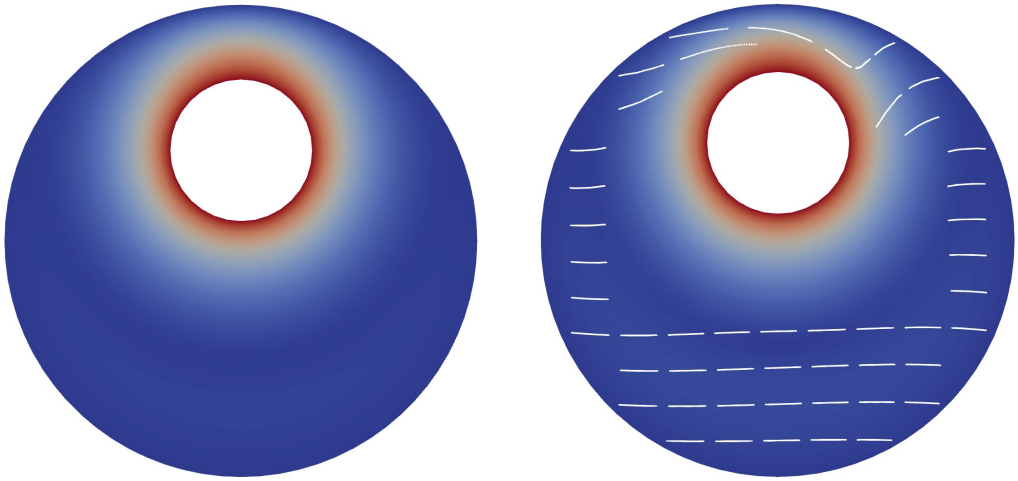

(a) $t = 0.2s$

(b) $t = 0.2s$

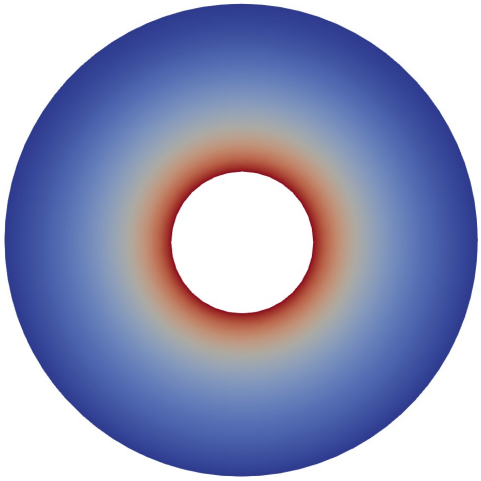

(c) $t = 0.4s$

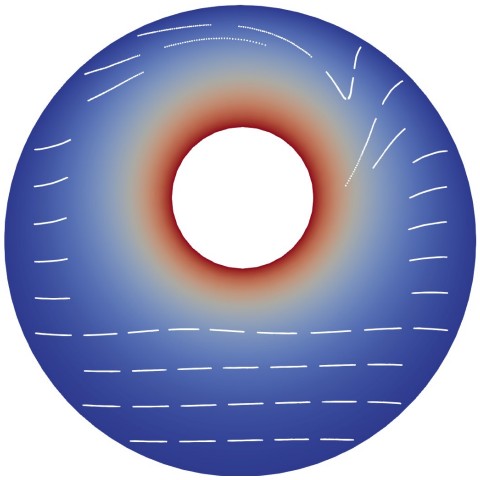

(d) $t = 0.4s$

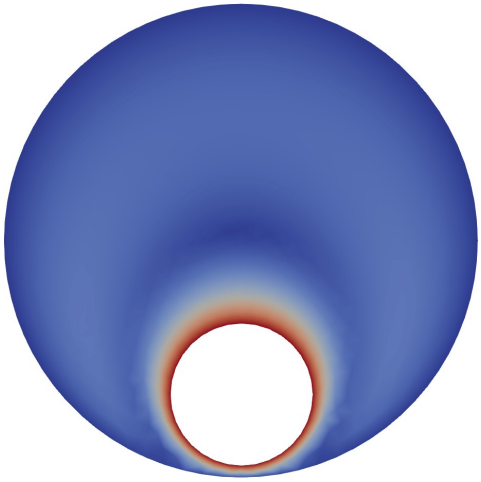

(e) $t = 0.6s$

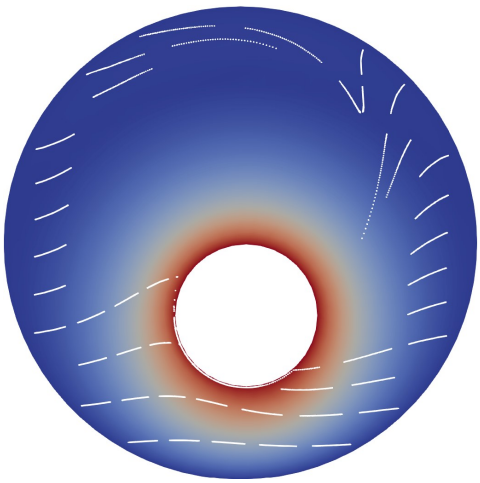

(f) $t = 0.6s$

Figure 4.17: Comparison of the evolution of the journal bearing without polymers (left) and with polymers (right) - Part 1.

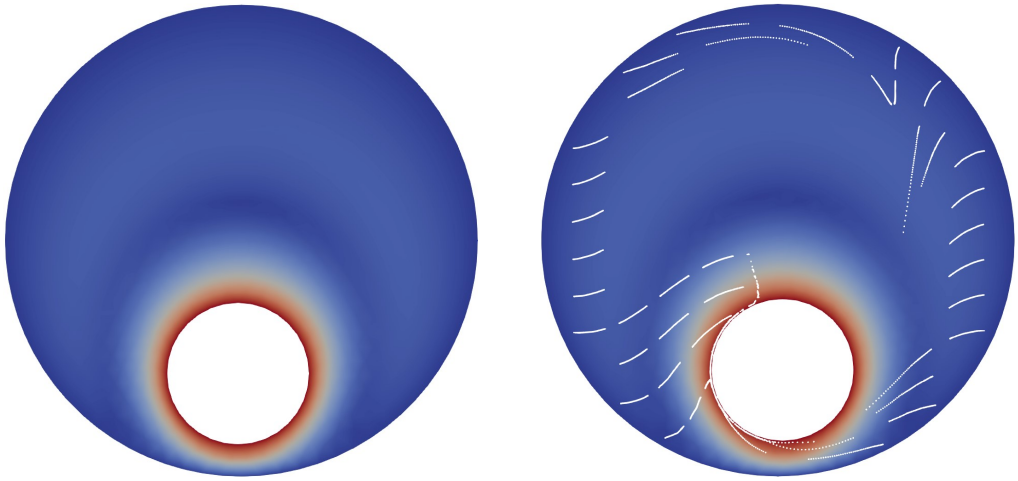

(a) $t = 0.8s$

(b) $t = 0.8s$

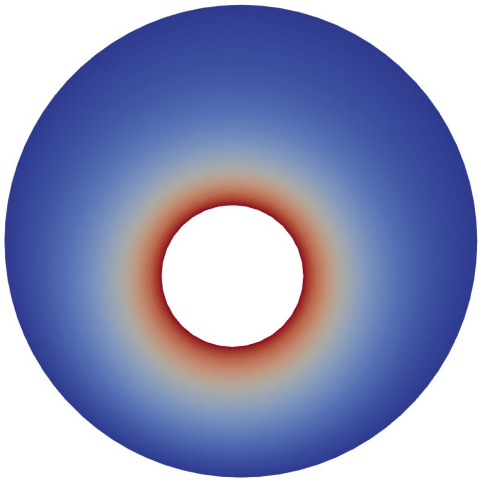

(c) $t = 1.0s$

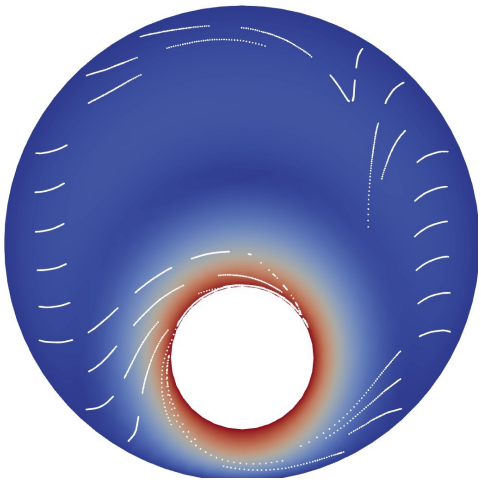

(d) $t = 1.0s$

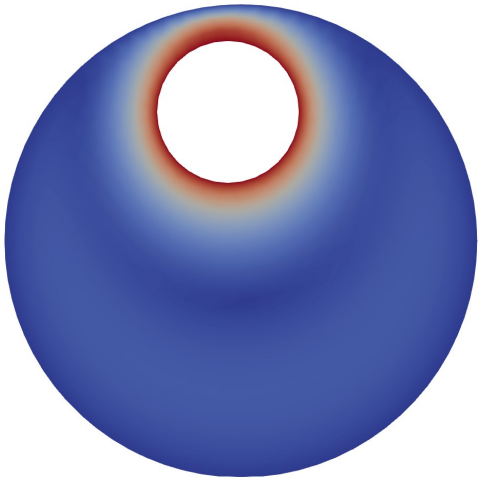

(e) $t = 1.2s$

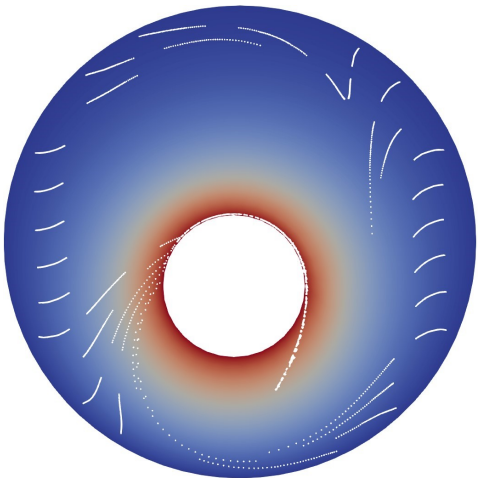

(f) $t = 1.2s$

Figure 4.18: Comparison of the evolution of the journal bearing without polymers (left) and with polymers (right) - Part 2.

4.8 Conclusion

We conclude this chapter with the knowledge that we have created a pertinent model capable of simulating the behaviours of a journal bearing assembly. Our model concurs with existing experimental and numerical data. Our simulations enable us to identify some of the parameters leading to instabilities. We are able to perform interesting stability studies and compare different lubricants, including lubricants with non-Newtonian properties. Both studies provide interesting insights that can be adapted to different industrial applications. Our simulations predict the behaviour of journal bearings and help in the choice of correct material and lubricant for given uses.

Chapter 5

Delayed die swell

The *die swell* or *Barus effect*, is a phenomenon that has been studied since the 1950s. As a viscoelastic fluid is expelled from a pipe, its behaviour is analysed. It has been found that its elastic properties induce a swell at the die lip. The first studies focused mainly on the kinematic aspects [44], however, these results did not fit with experimental data. This proves that other characteristics of the system needed to be considered.
In 1970, Grassley [45] identified additional parameters governing these swells: the geometry of the pipe, the characteristics of the fluids and external environmental parameters such as the pressure or gravity. Finally, in 1988, Koopmans [46] observed that polymers, more precisely their structure, also have an impact on the die swell.

At the same time, it was discovered that the swell becomes delayed for higher velocities. In 1987, the experiments of Joseph [47] studied and characterised this delay to isolate a critical velocity for different fluids and systems. The delay only appears if the Reynolds number is sufficiently high and the fluid is non-Newtonian. In 1990 the first numerical simulations of the delayed die swell were obtained using an Oldroyd-B model to describe non-Newtonian fluids [48].

While the Oldroyd-B model [49] simulates viscoelastic fluids, it does not consider the micro-scale properties of the polymers in the fluid and, as such, does not take into account the maximum extension of polymers. The purpose of this chapter is to study the delayed die swell with a multi-scale approach using a more advanced polymer model. This provides a more in-depth understanding of the mechanism at the origin of the delay and helps answer the open question of Brandt [50], which is to find the cause of the delayed die swell.

The first part of this chapter is dedicated to the physics of the *die swell* and the *delayed die swell*. The second part presents a simulation of the delayed die swell using the polymer model described in Chapter 2 and the moving boundaries from Chapter 3 in addition to a free surface implementation of *MigFlow*.

5.1 Physics of extrusion swelling

Let d be the diameter of a pipe in which a Poiseuille flow $u(x)$ is established. At the end of the pipe, there is an extrusion and the viscoelastic fluid swells up to a diameter D_1. This system is illustrated in Figure 5.1.

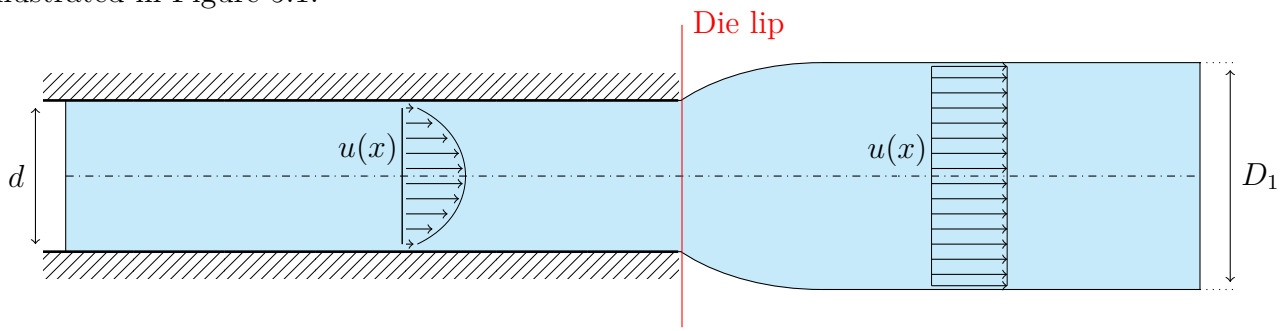

Figure 5.1: Illustration of the geometry of the die swell.

Both the Reynolds number (Re) and the Weissenberg number (We) are frequently used in non-Newtonian fluid dynamics and enable us to derive two non-dimensional numbers that describe the die swell:

- The elastic number $E = \frac{We}{Re}$ represents the ratio between the relaxation time and the time of observation.
- The viscoelastic Mach number $M = \sqrt{Re - We}$ is a normalised velocity of the system.

Delvaux and Crochet [48] hypothesised that the delay is solely dependent on the Mach number.

Adapting the Re and We enables us to reach the critical state where the die becomes delayed (see Figure 5.2). We see a first swell D_1 due to the *viscous* component of the fluid and a second D_2 due to its *elastic* component. This second swelling is delayed and can be seen as the consequence of the *memory* property of elastic bodies. The polymer chains are aligned with the streamline as they leave the die and take a certain amount of time before they change their configuration. In the following section, this phenomenon is simulated using our model to help understand the mechanisms in microscale at the origin of the delay.

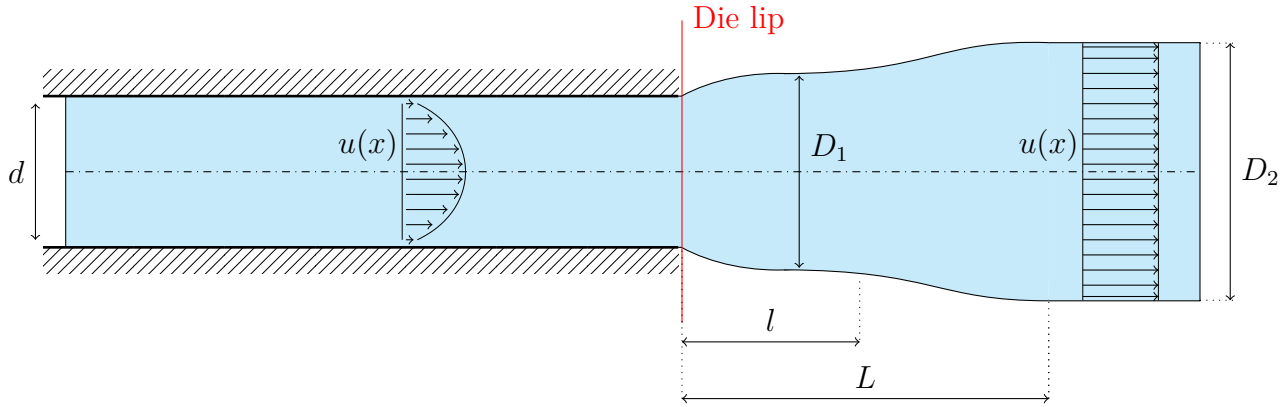

Figure 5.2: Illustration of the geometry of the delayed die swell.

The system is symmetrical along a horizontal axis represented by a *dotted and dashed* line in Figures 5.1 and 5.2. To reduce the computational costs, only the upper half of the geometry is simulated. Furthermore, this upper part can be assimilated to a shearing problem. At the die lip, the shear constraint disappears and the top boundary becomes a free surface. The velocity field homogenises when the fluid exits the pipe (once steady-state have been reached) as shown in Figure 5.3.

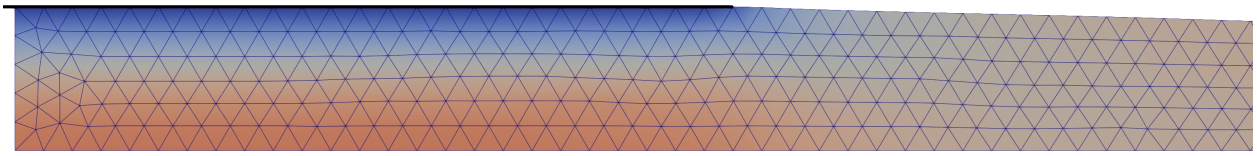

Figure 5.3: Velocity field around the die lip at steady state.

5.2 Simulation with polymeric fluid and moving boundaries

The polymer model described in Chapter 2 lets us simulate a non-Newtonian fluid with *Migflow*. An important aspect to consider is the appearance of a singularity at the die lip, between the pipe and the free surface. Though the singularity disappears as the solution converges, a sufficiently small time step has to be considered and the mesh needs a sufficiently high resolution. In practice, we use time step of $dt = 5 \cdot 10^{-5} s$ and the mesh is presented in Figure 5.6.

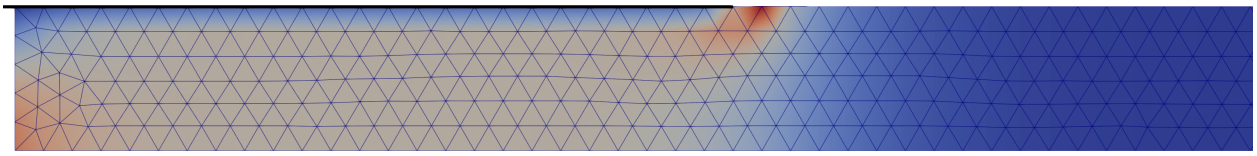

Figure 5.4: Velocity field around the die lip after the first iteration.

In Figure 5.4 we observe a high velocity (in the order of 8 times the shear velocity) at the die lip induced by the singularity. This creates a wave that propagates over time as shown in Figure 5.5.

Once the time step and the computational domain have been chosen, we move on to selecting the parameters required to simulate the delayed die swell. For this, we need a sufficiently high viscoelastic Mach number. Figure 5.5 shows an example with a Mach number of $M \approx 3.4$. In this figure, we see the evolution of the extrusion until it reaches a steady-state. At first, the extrusion creates a wave that propagates over the whole domain. The fluid then settles and at time ($t = 0.87s$) the flow is steady. We can see an initial small swell which is due to the viscosity of the fluid and then a second delayed swell.

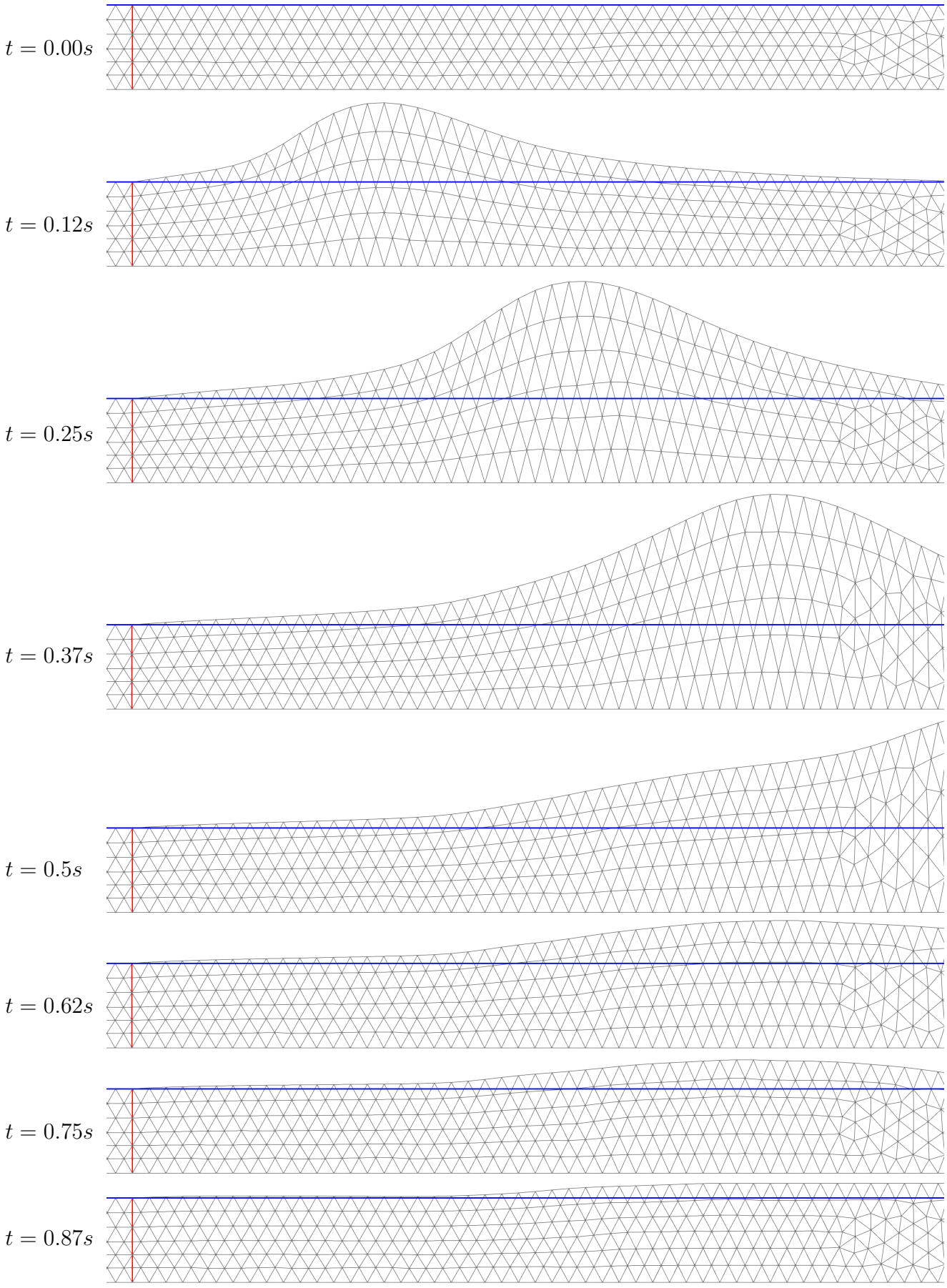

Figure 5.5: Simulation of a delayed die swell with a $Re = 12$ and $We = 0.42$. The red line corresponds to the end of the pipe and the blue line is a reference line that corresponds to the radius of the pipe.

Now that we can produce a delayed die swell, we can explore variations by modifying non-dimensional numbers and observing their impact. Table 5.1 shows a summary of the non-dimensional numbers used in our simulations.

Set	1	2	3	4
Re	12	24	16	12
We	0.42	0.5	0.73	0.7
M	3.4	4.85	3.9	3.36
E	0.035	0.02	0.046	0.058

Table 5.1: Non-dimensional numbers used for simulations.

To modify these numbers, several parameters can be varied: the viscosity, the length of the polymers, the strength of the joints and the size of the particles.
In practice, we observe that the linear momentum of the particles seems to be the cause of the delayed die swell. We have therefore chosen not to alter the velocity of the fluid or the mass of the particles in these simulations.

The four stationary solutions corresponding to the tests are shown in Figure 5.6

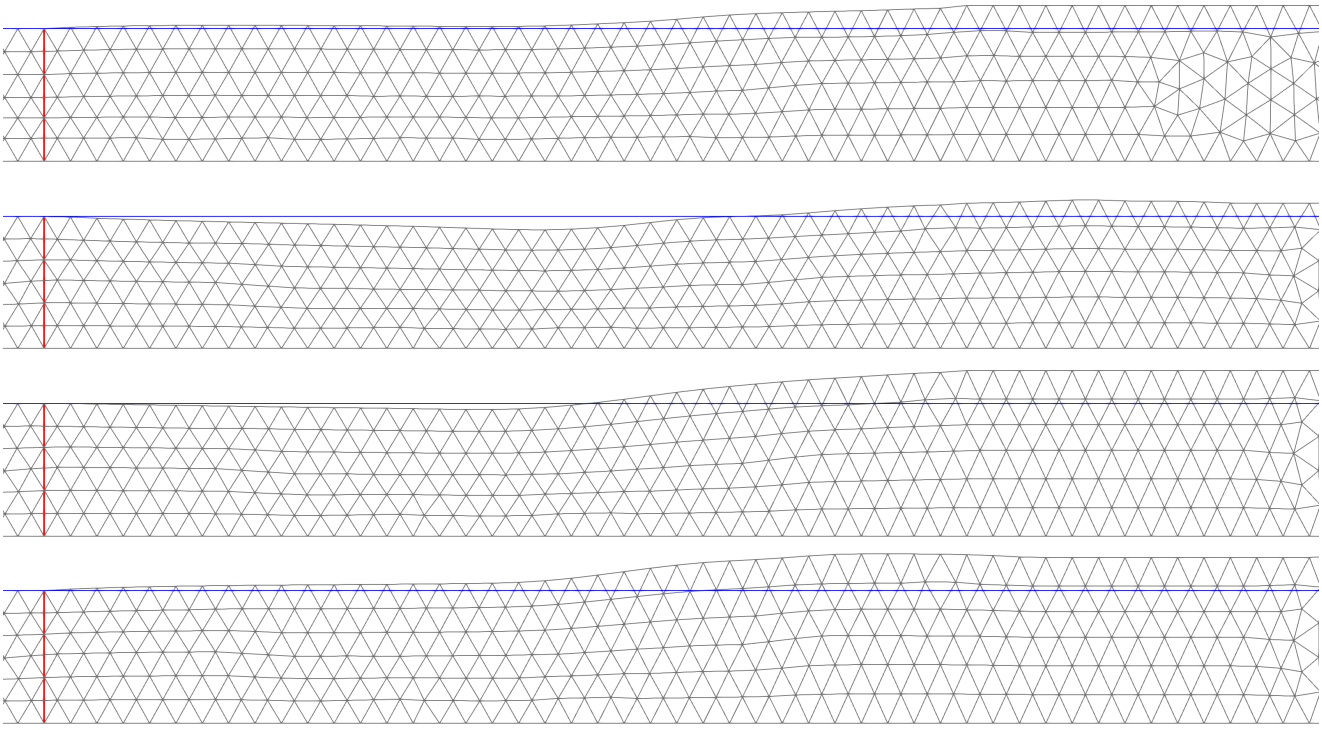

Figure 5.6: Resulting mesh of the delayed die swell simulation corresponding to Table 5.1. The red line corresponds to the end of the pipe and the blue line is a reference line that corresponds to the radius of the pipe.

We observe two main trends.
First, when increasing the Re, the first swell *decreases* until eventually, a narrowing occurs. This is due to the reduction in the viscosity needed to achieve these high Re numbers.
Secondly, increasing the We *increases* the second swell D_2.

We can postulate that the ratio between the first and the second swelling is directly proportional to the Reynolds and Weissenberg numbers of a fluid. Mathematically, this would give:

$$\frac{D_2}{D_1} \propto Re \cdot We \tag{5.1}$$

5.3 Micro-scale analysis

As we stated previously, the advantage of using a micro-macro (multi-scale) model is to allow us to observe the behaviour of the polymers during the delayed die swell.
In the simulations, each chain represents a set of polymers. This has the advantage of reducing computational costs while giving good qualitative results. Quantitative results are not considered in this paper and the scales do not correspond to any applications but are specifically chosen to help us understand the intrinsic mechanisms of non-Newtonian fluids.

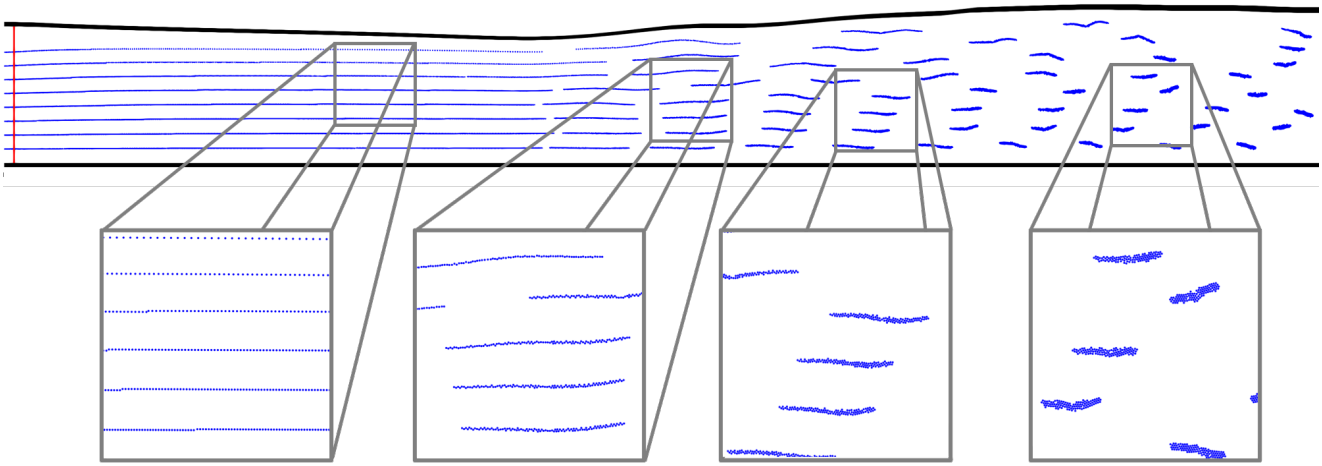

Figure 5.7: Evolution of the shape of the polymers along the flow.

We can see in Figure 5.7 the evolution of the shape of polymers throughout the flow. The polymers tend to curl (as described in Chapter 2) but only after a delay. This is the origin of the delayed die swell and is due to the inertia of the particles.
We assume that the pipe is sufficiently long such that the velocity of the particles equals the velocity of the fluid at all points. The particles have a higher density than the fluid and, as such, for the same velocity, their linear momentum is higher. At the die lip, the constraints of the shearing flow disappear. The higher linear momentum of the particles keeps them in their linear shape for a certain amount of time, during which the Brownian motion is dominated by the velocity of the particles. This creates a delay until their velocity decreases to that of the fluid and the Brownian motion is no longer negligible. After this delay, the polymers will start to curl and assume their dense shape as seen in Figure 5.7.

Therefore, we observe a delayed die swell if the linear momentum of the particles is sufficiently high. The other parameters cause variations to the steady-state solution. Modifying the Re and the We will change the first and the second swellings accordingly.

5.4 Conclusion

In the final results, we recompose the entire domain using symmetry. The full delayed die swell is shown in Figure 5.8.

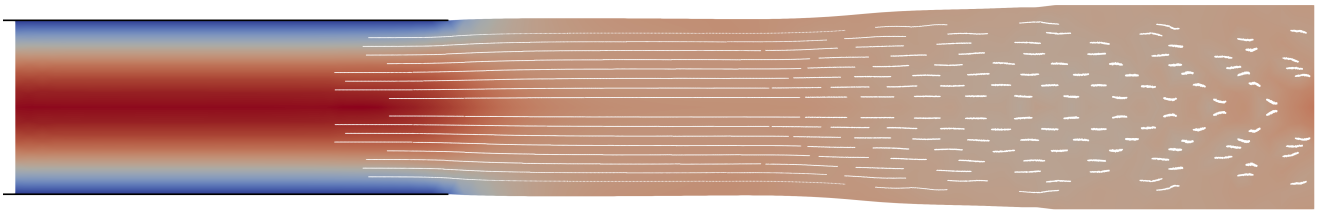

Figure 5.8: Delayed die swell simulation.

In this figure, we see a Poiseuille flow is established in the pipe. A first small swell is observed at the die lip, followed by a second swell that is delayed. This figure shows the behaviours of the polymer chains throughout the domain and we observe how the curling action induces the second delayed swell.
It is important to note that these results are qualitative due to our multiscale approach. Our objective is to answer the open question on the cause of the delayed die swell. Based on our results, we can formulate the hypothesis that the delayed die swell is due to the balance between the linear momentum of the polymer and the Brownian motion they are subjected to.
These simulations can also be considered as a basis for further simulations and studies. For example, analysis can be performed on the position of the inflection point or different types of polymers using our model.

Chapter 6

Conclusion

This paper is based on the *Migflow* (**M**odel for **I**mmersed **G**ranular **Flow**s) project where we aimed to research and develop two major enhancements. We also provided concrete applications and case studies to validate our findings and explore the possibilities of our models. The first enhancement was the implementation of immersed polymers enabling us to study the mechanisms at the origin of the non-Newtonian behaviour of polymeric fluids. The second focused on creating a methodology to handle adaptive geometries, allowing us to consider complex domains.

First, a polymer model is described and implemented. This makes it possible to simulate polymeric fluids and to observe the microscopic mechanisms causing unusual non-Newtonian behaviours. These fluids are viscoelastic and, as such, we must research and develop an elastic model for our polymer chains. We have studied the impact of two elastic models: a simple and widely used model based on Hooke's law and a second that considers the maximum extension of bodies, based on the FENE model. Both models were implemented and compared. It was found that the adapted FENE model is better suited for a larger range of applications as it is accurate for both small and large deformations. We have therefore chosen the FENE model for our research.
It is known that the structure of polymers has an important impact on the fluid. As polymers forming complex networks are rarely found in a fluid phase, our work focuses on chained polymers, both linear and branched. We proposed two representations for the structure of polymers according to their physical properties. The chain representation can be used to simulate large polymers that don't have a defined shape while the triangular representation is more appropriate for smaller polymers with a given shape. Both representations are created using a scale analogy where each chain represents several microscopic polymers but behaves as a single microscopic polymer. This analogy enables us to observe the macroscopic behaviour induced by polymers in a reasonable computational time.
Future studies into more complex structures (e.g. polymer networks) could be implemented using our model to simulate more elaborate fluids.

The second enhancement is a method to handle moving boundaries. Many problems in fluid mechanics require dynamic domains in which boundaries shift or evolve. This paper proposes a complete methodology to take this into account. First, the mesh used by the finite element scheme of *Migflow* is adapted according to the displacement of the boundaries. The solution of the different fields is recomputed on the adapted mesh. We encountered two cases. First, in the case of small deformations, the position of the nodes are adapted and we use the Euler-Lagrange approach to calculate the various fields such as velocity and pressure. Secondly, in the case of large

deformations, we have to re-mesh the whole domain and project the old fields on the new mesh. Although both methods impact the performance of *MigFlow*, they do not impact the global temporal complexity of the program.
Using these moving boundaries allows us to consider a new range of problems in which the geometry evolves or where bodies are free to move within the domain.

The subsequent chapters are dedicated to concrete applications of these enhancements in which we study and provide illustrations of the capabilities of our model. The first application provides quantitative results and compares these to external studies. The second provides qualitative results to answer open questions in physics (such as the causes of the delayed die swell).

The first application is the study of journal bearings. These simulations validate the methodology used for our moving boundaries by comparing our results with external numerical and experimental data. Our results and conclusions are very promising and are in agreement with scientific literature. Various cases are simulated to study the impact of the different parameters on the stability of the bearing and observe its response to perturbations.
Finally, polymers are introduced into the clearance to compare Newtonian and non-Newtonian lubricants. Our results concur once again with experimental data, confirming the pertinence of our model.

The second application is the study of the delayed die swell. This phenomenon occurs (in specific conditions) when a non-Newtonian fluid is expelled from a pipe. The nature of the microscopic mechanisms causing this behaviour remains an open question.
To answer this, we propose a micro-macro approach to gain a deeper understanding of the inner mechanisms at the origin of this behaviour. Our enhancements are used to simulate the delayed die swell. By observing the behaviours of the polymers during the second swell, we were able to postulate that the delay is due to the linear momentum of the polymers which dominates their tendency to curl for a certain amount of time.
An analysis has been performed in an attempt to identify the parameters governing the delayed die swell. Further studies may be carried out, for example, focusing on the inflection point and its position.
Our work on the delayed die swell can be generalised to a multitude of other problems.

Our enhancements add new perspectives to the *Migflow* software and can be used in many and varying applications. We provided concrete examples of how they can be applied. They enable the simulation of more complex problems with dynamic domains and non-Newtonian fluids while providing in-depth visualisations and understanding of these non-Newtonian fluids.

Appendices

A Hooke's law & potential energy

There is a clear link between potential energy and Hooke's law. Let us define $U(x)$ as the potential energy that poses a local minimum at $x^\star$.
The Taylor expansion around this point is defined as:

$$U(x) = \sum_{n=0}^{\infty} U_n (x - x^\star)^n = U_0 + U_1(x - x^\star) + U_2(x - x^\star)^2 + ...$$

Considering small deformations, we may focus on the first terms of the Taylor expansion.

The very first term is constant and can be assumed to be $U_0 = 0$ without loss of generality (this corresponds to a shift in the potential energy). The second term U_1 is the value of the derivative of the potential energy when there is no extension : $U_1 = \frac{dU}{dx}(x^\star)$. Since we know the potential energy is minimum at this point, $U_1 = 0$. The third term is, with the same reasoning, the second derivative : $U_2 = \frac{1}{2}\frac{d^2U}{dx^2}(x^\star) \equiv \frac{1}{2}k \geq 0$ for an arbitrary potential energy[1]. Indeed $\frac{d^2U}{dx^2} = 2U_2 + 6U_3(x - x^\star) + ...$ so by taking the rest point $x = x^\star$ we have only the U_2 term remaining.

Keeping only the first non-zero term (U_2), we have:

$$U(x) \approx \frac{1}{2}k(x - x^\star)^2$$

By deriving this expression, we find the force induced on the solid:

$$F = -\frac{dU(x)}{dx} \approx -k(x - x^\star)$$

This is the same expression as Hooke's law, where k is the spring constant and $x^\star$ is the resting length.

[1] In some particular cases of potential energy function this term could vanish too but in practice it is not considered.

B Stenosis

A stenosis is an anatomical narrowing of part of a biological system. In the human body it is found for example in the respiratory voices or in the vascular system [51] [52]. They can be at the origin of vascular disorder and have important consequences for the biological system hosting the stenosis [53].
The human vascular system (can be generalised to other species) is made up of a network of arteries and veins in which a non-Newtonian fluid, blood, evolves. A stenosis in this system can have serious consequences for its host and therefore it can be very interesting to understand and predict its consequences. Another approach would be to study the impact of medicine (coagulant or anticoagulant, for example) on this stenosis and its consequence.

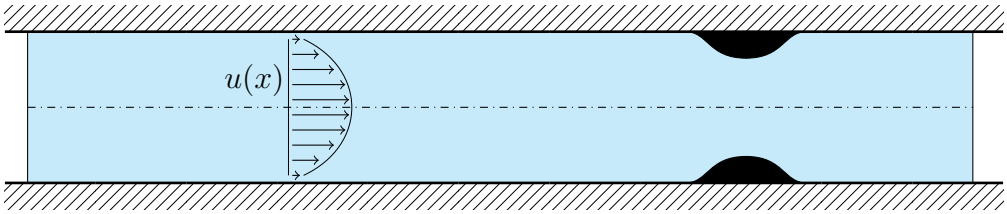

Figure B.1: Illustration of a stenosis into a pipe in which a Couette flow $u(x)$ is established.

A very simplified model for showing stenosis is shown in Figure B.1. This model represents a section of a blood vessel in which a substantial irregularity appears (the stenosis).
Using the tools developed in this paper, we can therefore simulate the impact of this stenosis on the non-Newtonian fluid as well as the different components of this fluid. We can also simulate pulsation on the stenosis by using the dynamic boundaries method developed in Chapter 3 [54].
As blood rheology is a very complex subject, an implementation will not be proposed but this appendix illustrates a potential application of our model in a field very different from industry.

C OCTree

An OCTree is a tree-based structure used to store nodes in space. It is often considered as the 3D version of the quadtree. This structure divides the space in elements and each elements can be divided into a sub-space of 8 elements (4 for a quadtree) and this can continue recursively. An illustration of this concept can be found in Figure C.1.

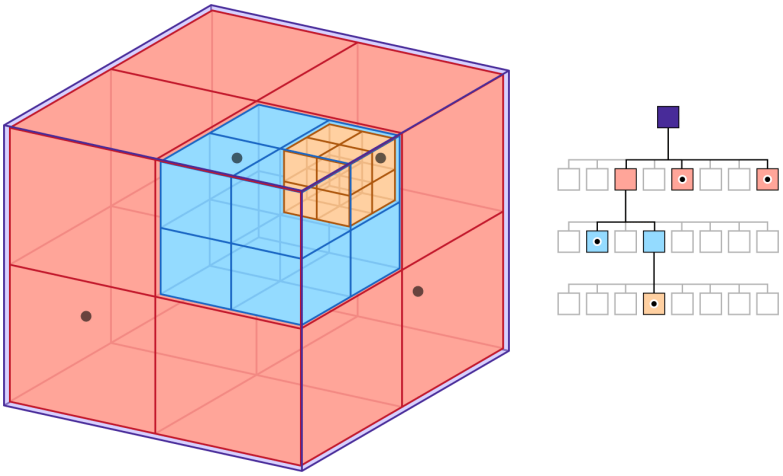

Figure C.1: OCTree representation [2].

For N points evenly distributed in the space (i.e. a well balanced tree) the cost of search and insertion of one point is $\mathcal{O}(\log N)$.

[2]Source: https://developer.apple.com/documentation/gameplaykit/gkoctree

D Magnetic stirrer

A magnetic stirrer is a device mainly used in chemistry or biology laboratories. This device is composed of 2 parts : a magnetic bar and a base. In the base, a magnet, called the drive magnet, turns the magnetic bar.
The device is used to mix liquid solutions in a recipient. The user places the magnetic bar into the recipient with the fluid and puts the recipient on the base. Then, the drive magnet starts to spin, causing the magnetic bar to mix the solution.
A scheme can be observed in Figure D.2. D.2.

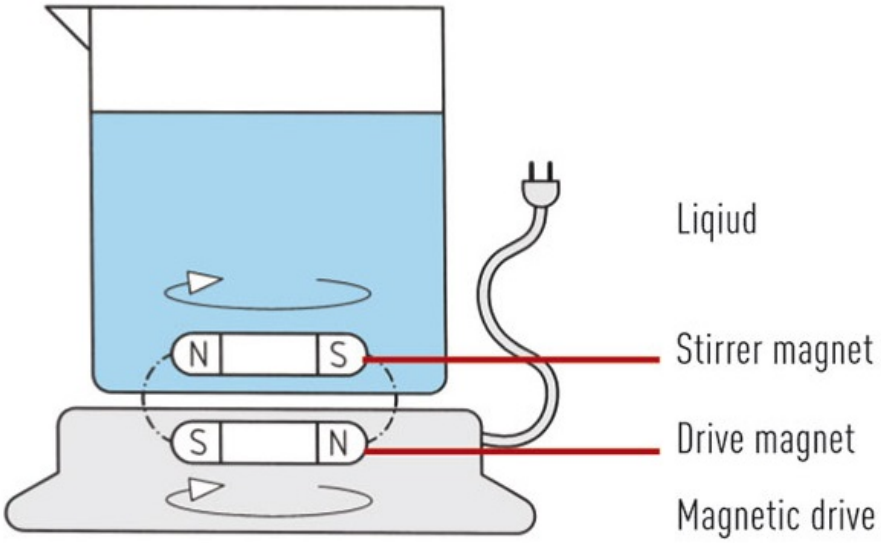

Figure D.2: Magnetic stirrer scheme[3].

In the Chapter 3, this system is simulated in 2D. So only a section is considered. This section is the horizontal plane going through the stirrer magnet. An illustration of the geometry can be found in Figure 3.1.

[3]Source: https://www.bola.de/en/technical-information/stirring-and-mixing/stirrer-magnetic-stirring/

E Magnetic stirrer simulation with polymers

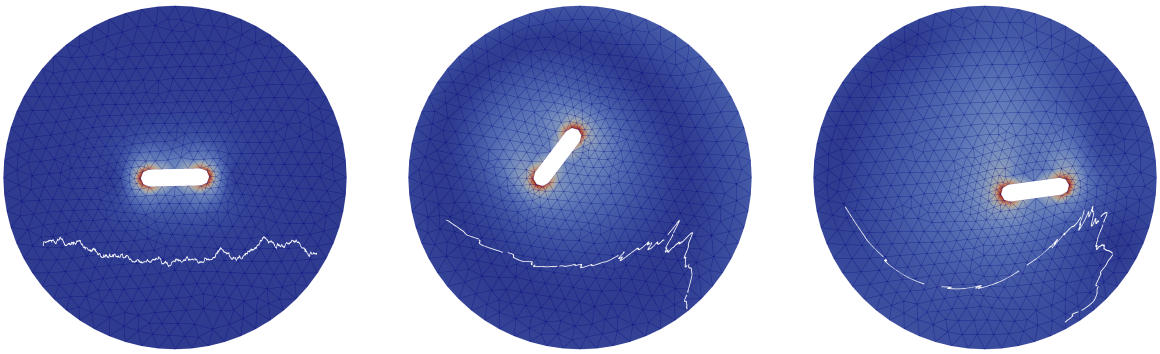

(a) $t = 0.1s$ (b) $t = 0.2s$ (c) $t = 0.3s$

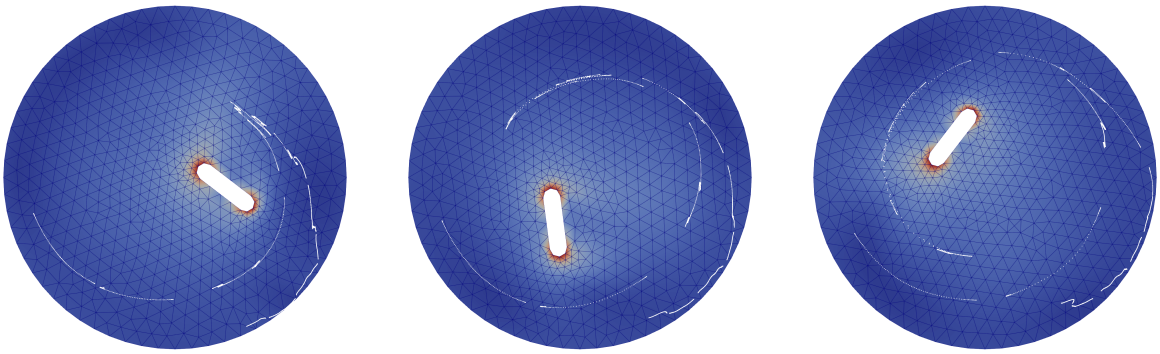

(d) $t = 0.4s$ (e) $t = 0.5s$ (f) $t = 0.6s$

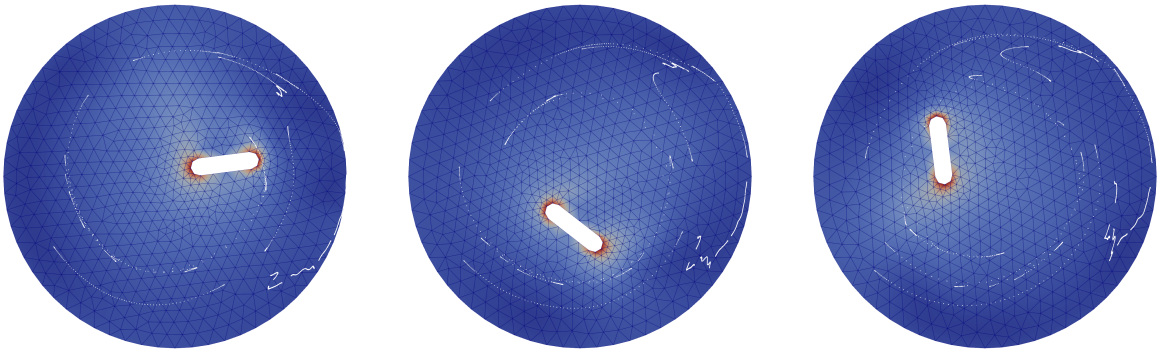

(g) $t = 0.7s$ (h) $t = 0.8s$ (i) $t = 0.9s$

Figure E.3: Full simulation of a magnetic stirrer.

F Simulation of a journal bearing with polymers

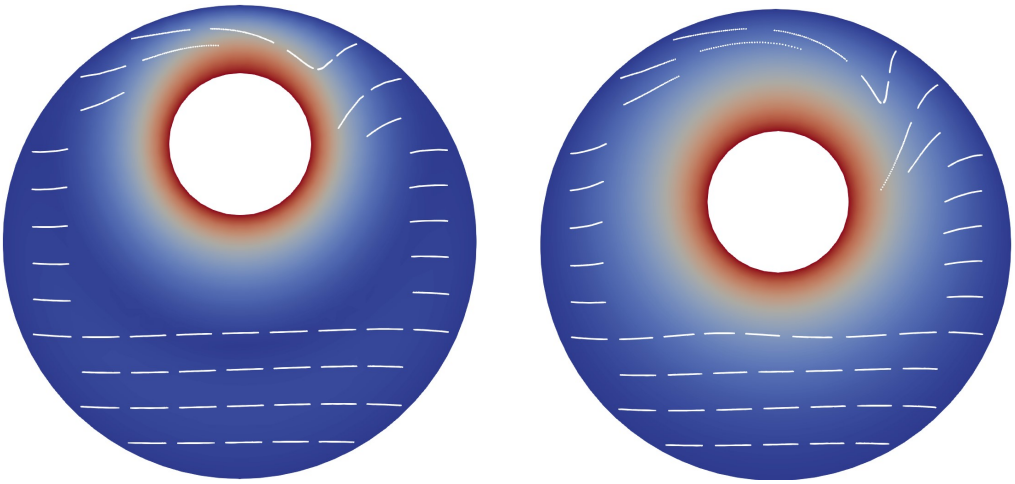

(a) $t = 0.2$

(b) $t = 0.4s$

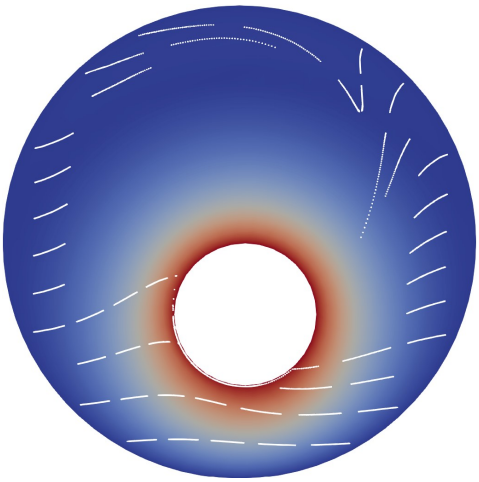

(c) $t = 0.6s$

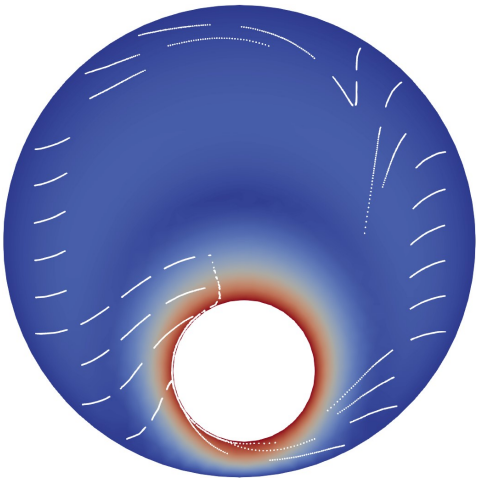

(d) $t = 0.8s$

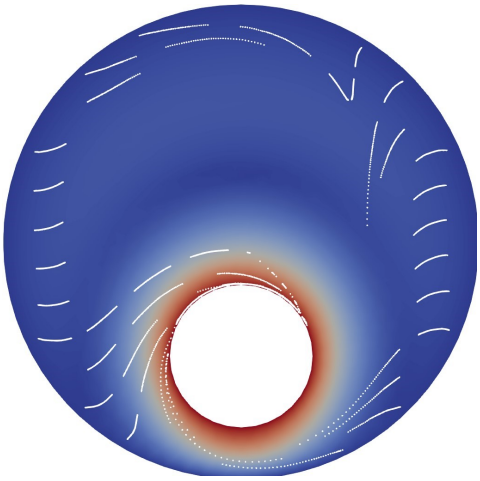

(e) $t = 1.0s$

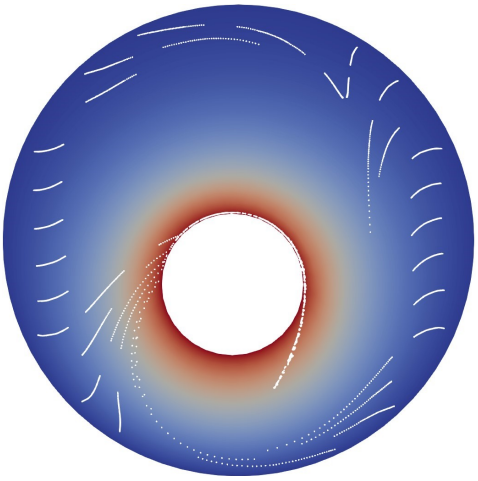

(f) $t = 1.2s$

Figure F.4: Full simulation of a journal bearing with polymer chains (Part 1).

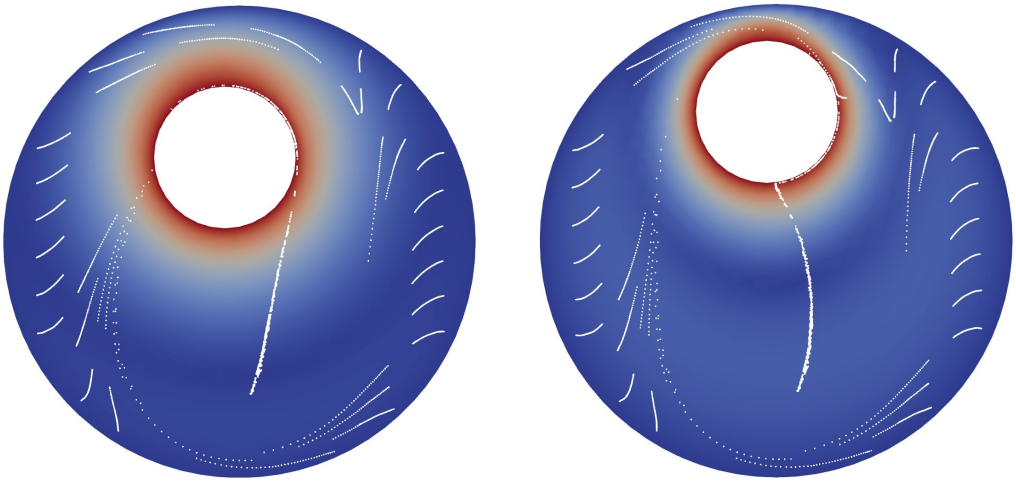

(a) $t = 1.4s$

(b) $t = 1.6s$

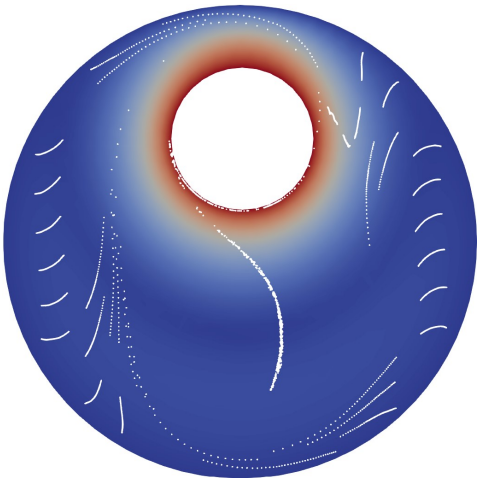

(c) $t = 1.8s$

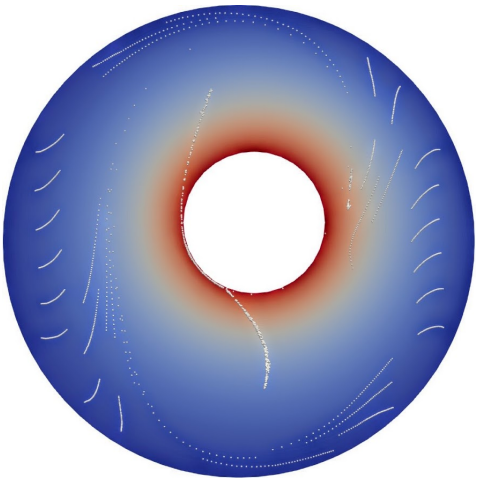

(d) $t = 2.0s$

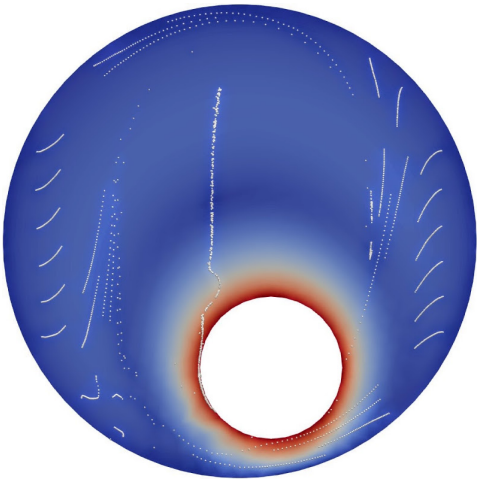

(e) $t = 2.2s$

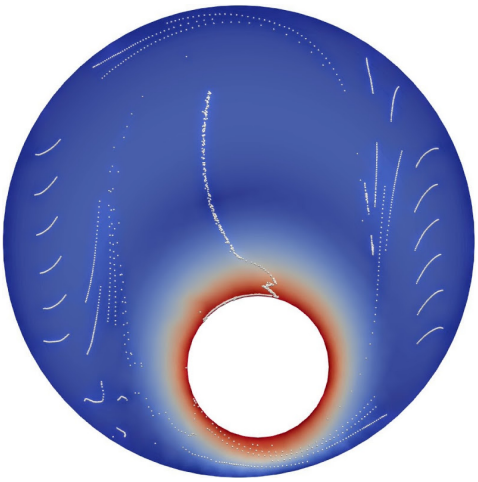

(f) $t = 2.4s$

Figure F.5: Full simulation of a journal bearing with polymer chains (Part 2).

G Simulation of a stable journal bearing with a vortex

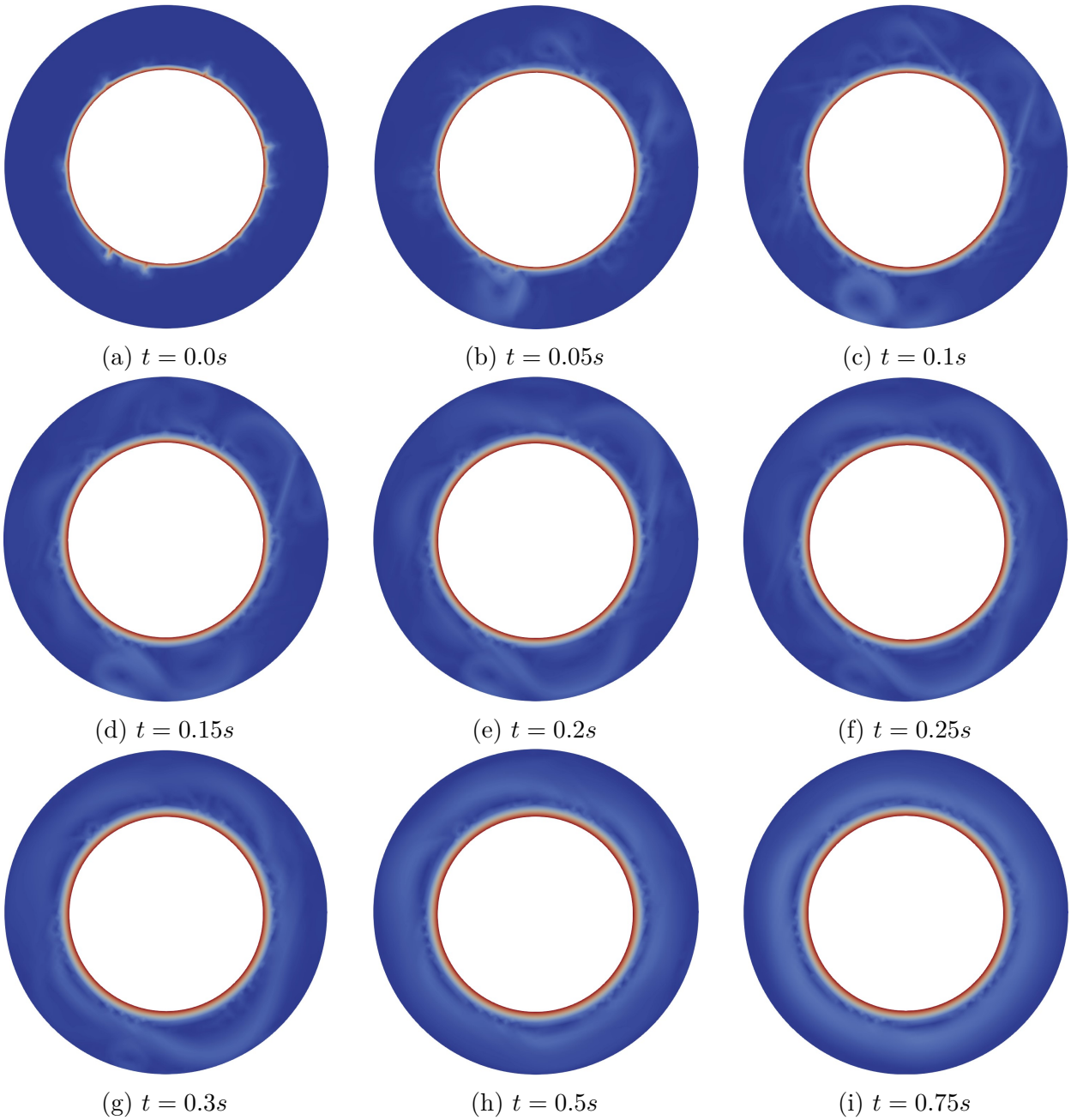

(a) $t = 0.0s$ (b) $t = 0.05s$ (c) $t = 0.1s$

(d) $t = 0.15s$ (e) $t = 0.2s$ (f) $t = 0.25s$

(g) $t = 0.3s$ (h) $t = 0.5s$ (i) $t = 0.75s$

Figure G.6: Full simulation of the stable journal bearing.

Bibliography

[1] R. Temam, *Navier-Stokes equations: theory and numerical analysis*. American Mathematical Soc., 2001, vol. 343.

[2] D. Qian, L. Ye, M. Zhang, Y. Liang, L. Li, Y. Huang, X. Guo, S. Zhang, Z. Tan, and J. Hou, "Design, application, and morphology study of a new photovoltaic polymer with strong aggregation in solution state," *Macromolecules*, vol. 45, no. 24, pp. 9611–9617, 2012.

[3] H. Singh and F. MacRitchie, "Application of polymer science to properties of gluten," *Journal of Cereal Science*, vol. 33, no. 3, pp. 231–243, 2001.

[4] N. Breidenbach, C. Martin, H. Jockenhöfer, and T. Bauer, "Thermal energy storage in molten salts: Overview of novel concepts and the dlr test facility (tesis)," 2016.

[5] P. N. Haubenreich and J. Engel, "Experience with the molten-salt reactor experiment," *Nuclear Applications and technology*, vol. 8, no. 2, pp. 118–136, 1970.

[6] D. S. Manju Rawat Singh Satish Patel, "Natural polymer-based hydrogels as scaffolds for tissue engineering," *Applications of Nanobiomaterials*, vol. 5, pp. 231–260, 2016.

[7] P. S. Doyle and P. T. Underhill, "Brownian dynamics simulations of polymers and soft matter," in *Handbook of materials modeling*, Springer, 2005, pp. 2619–2630.

[8] A. A. Gusev and F. Schwarz, "Molecular dynamics validation and applications of the maximum entropy homogenization procedure for predicting the elastic properties of gaussian polymer networks," *Macromolecules*, vol. 52, no. 24, pp. 9445–9455, 2019.

[9] A. C. Ugural and S. K. Fenster, *Advanced strength and applied elasticity*. Pearson education, 2003.

[10] G. Marrucci, "The free energy constitutive equation for polymer solutions from the dumbbell model," *Transactions of the Society of Rheology*, vol. 16, no. 2, pp. 321–330, 1972.

[11] S. Jin and L. R. Collins, "Dynamics of dissolved polymer chains in isotropic turbulence," *New Journal of Physics*, vol. 9, no. 10, p. 360, 2007.

[12] J. Englander, "Particle models with interaction through the center of mass," 2011.

[13] R. B. Bird, R. C. Armstrong, and O. Hassager, "Dynamics of polymeric liquids. vol. 1: Fluid mechanics," 1987.

[14] H. K. Rasmussen, J. K. Nielsen, A. Bach, and O. Hassager, "Viscosity overshoot in the start-up of uniaxial elongation of low density polyethylene melts," *Journal of Rheology*, vol. 49, no. 2, pp. 369–381, 2005.

[15] G. Russell, "The size and shape of a polymer molecule," [Online]. Available: `https://research.csiro.au/crystal/the-size-and-shape-of-a-polymer-molecule/`.

[16] P. Attard, *Thermodynamics and statistical mechanics: equilibrium by entropy maximisation*. Academic Press, 2002.

[17] M. E. Gurtin, *An introduction to continuum mechanics*. Academic press, 1982.

[18] C. Geuzaine and J.-F. Remacle, "Gmsh: A 3-d finite element mesh generator with built-in pre- and post-processing facilities," *International journal for numerical methods in engineering*, vol. 79, no. 11, pp. 1309–1331, 2009.

[19] J. Capecelatro and O. Desjardins, "An euler–lagrange strategy for simulating particle-laden flows," *Journal of Computational Physics*, vol. 238, pp. 1–31, 2013.

[20] G. Mathew, I. Mezić, and L. Petzold, "A multiscale measure for mixing," *Physica D: Nonlinear Phenomena*, vol. 211, no. 1-2, pp. 23–46, 2005.

[21] K. Brun and R. Kurz, *Compression Machinery for Oil and Gas*. Elsevier Science, 2018, ISBN: 9780128146842. [Online]. Available: `https://books.google.be/books?id=4OR8DwAAQBAJ`.

[22] T. Tanuma, *Advances in Steam Turbines for Modern Power Plants*, ser. Woodhead Publishing Series in Energy. Elsevier Science, 2017, ISBN: 9780081003251. [Online]. Available: `https://books.google.be/books?id=IoV4CgAAQBAJ`.

[23] H. Rahnejat, *Tribology and Dynamics of Engine and Powertrain: Fundamentals, Applications and Future Trends*, ser. Woodhead Publishing in mechanical engineering Tribology and dynamics of engine and powertrain. Elsevier Science, 2010, ISBN: 9781845699932. [Online]. Available: `https://books.google.be/books?id=vJJwAgAAQBAJ`.

[24] A. Sommerfeld, "Zur hydrodynamischen therorie der schmiermittelreibung," *Z. Math. Phys.*, p. 97, 1904.

[25] W. J. Harrison, "The hydronamical theory of lubrication with special reference to air as lubricant," *Trans Cambrige Phil Soc*, p. 39, 1913.

[26] C. D., "A new mathematical method for the solution of film lubrication problems," *Proc. Inst. Mech. Engrs. (London)*, vol. 146, p. 126, 1942.

[27] R. A., "A solution for the finite journal bearing and its application to analysis and design," *Trans. ASLE*, vol. 1, p. 159, 1958.

[28] A. Raimondi, "A numerical solution for the gas lubricated full journal bearing of finite length," *ASLE TRANSACTIONS*, vol. 4, no. 1, pp. 131–155, 1961.

[29] S. Heller and W. Shapiro, "A numerical solution for the incompressible hybrid journal bearing with cavitation," 1969.

[30] M. B. Aitken and H. McCallion, "Elastohydrodynamic lubrication of big-end bearings part 1: Theory," *Proceedings of the Institution of Mechanical Engineers, Part C: Mechanical Engineering Science*, vol. 205, no. 2, pp. 99–106, 1991. DOI: `10.1243/PIME\_PROC\_1991\_205\_097\_02`. eprint: `https://doi.org/10.1243/PIME_PROC_1991_205_097_02`. [Online]. Available: `https://doi.org/10.1243/PIME_PROC_1991_205_097_02`.

[31] H. Heshmat, "The mechanism of cavitation in hydrodynamic lubrication," *Tribol. Trans.*, no. 34, pp. 177–186, 1991.

[32] S. Poddar and N. Tandon, "Detection of journal bearing vapour cavitation using vibration and acoustic emission techniques with the aid of oil film photography," *Tribology International*, vol. 103, pp. 95–101, 2016, ISSN: 0301-679X. DOI: https://doi.org/10.1016/j.triboint.2016.06.039. [Online]. Available: https://www.sciencedirect.com/science/article/pii/S0301679X16302109.

[33] D. F. Hays, "A variational approach to lubrication problems and the solution of the finite journal bearing," *Journal of Basic Engineering*, vol. 81, no. 1, pp. 22–23, Mar. 1959, ISSN: 0021-9223. DOI: 10.1115/1.4008348. eprint: https://asmedigitalcollection.asme.org/fluidsengineering/article-pdf/81/1/22/6186237/22_1.pdf. [Online]. Available: https://doi.org/10.1115/1.4008348.

[34] "Ansys fluent 12.0 user's guide," [Online]. Available: https://www.afs.enea.it/project/neptunius/docs/fluent/html/ug//main_pre.htm.

[35] H. Jasak, "Openfoam: Open source cfd in research and industry," *International Journal of Naval Architecture and Ocean Engineering*, vol. 1, no. 2, pp. 89–94, 2009.

[36] E. S. Piekos, "Numerical simulation of gas-lubricated journal bearings for microfabricated machines," Ph.D. dissertation, Massachusetts Institute of Technology, 2000.

[37] K. Gertzos, P. Nikolakopoulos, and C. Papadopoulos, "Cfd analysis of journal bearing hydrodynamic lubrication by bingham lubricant," *Tribology International*, vol. 41, no. 12, pp. 1190–1204, 2008.

[38] B. A. Gecim, "Non-newtonian effects of multigrade oils on journal bearing performance," *Tribology transactions*, vol. 33, no. 3, pp. 384–394, 1990.

[39] A. Beris, R. Armstrong, and R. Brown, "Finite element calculation of viscoelastic flow in a journal bearing: Ii. moderate eccentricity," *Journal of non-newtonian fluid mechanics*, vol. 19, no. 3, pp. 323–347, 1986.

[40] E. Okrent, "The effect of lubricant viscosity and composition on engine friction and bearing wear," *ASLE TRANSACTIONS*, vol. 4, no. 1, pp. 97–108, 1961.

[41] E. Stanley, "Numerical simulation of gas-lubricated journal bearings for microfabricated machines," *Thesis (Ph.D.)–Massachusetts Institute of Technology, Dept. of Aeronautics and Astronautics*, 2000. [Online]. Available: http://hdl.handle.net/1721.1/16738.

[42] A. Berker, M. Bouldin, S. Kleis, and W. VanArsdale, "Effect of polymer on flow in journal bearings," *Journal of non-newtonian fluid mechanics*, vol. 56, no. 3, pp. 333–347, 1995.

[43] A. Rastogi and R. Gupta, "Lubricant elasticity and the performance of dynamically loaded short journal bearings," *Journal of Rheology*, vol. 34, no. 8, pp. 1337–1356, 1990.

[44] W. Philippoff and F. H. Gaskins, "The capillary experiment in rheology," *Transactions of the Society of Rheology*, vol. 2, no. 1, pp. 263–284, 1958.

[45] W. W. Graessley, S. D. Glasscock, and R. L. Crawley, "Die swell in molten polymers," *Transactions of the Society of Rheology*, vol. 14, no. 4, pp. 519–544, 1970.

[46] R. Koopmans, "Die swell–molecular structure model for linear polyethylene," *Journal of Polymer Science Part A: Polymer Chemistry*, vol. 26, no. 4, pp. 1157–1164, 1988.

[47] D. D. Joseph, J. E. Matta, and K. Chen, "Delayed die swell," *Journal of non-newtonian fluid mechanics*, vol. 24, no. 1, pp. 31–65, 1987.

[48] V. Delvaux and M. Crochet, "Numerical simulation of delayed die swell," *Rheologica acta*, vol. 29, no. 1, pp. 1–10, 1990.

[49] J. G. Oldroyd, "On the formulation of rheological equations of state," *Proceedings of the Royal Society of London. Series A. Mathematical and Physical Sciences*, vol. 200, no. 1063, pp. 523–541, 1950.

[50] C. D. L. Brandt. (). "Delayed die swell," [Online]. Available: `https://www.mech.kth.se/~luca/html_lib/dieswell.html`. (accessed: 10.02.2021).

[51] J. Ross Jr and E. Braunwald, "Aortic stenosis," *Circulation*, vol. 38, no. 1s5, pp. V–61, 1968.

[52] B. A. Carabello and W. J. Paulus, "Aortic stenosis," *The lancet*, vol. 373, no. 9667, pp. 956–966, 2009.

[53] V. K. Tanguturi, B. R. Lindman, P. Pibarot, J. J. Passeri, S. Kapadia, M. J. Mack, I. Inglessis, N. B. Langer, T. M. Sundt, J. Hung, *et al.*, "Managing severe aortic stenosis in the covid-19 era," *JACC: Cardiovascular Interventions*, 2020.

[54] C. Tu, M. Deville, L. Dheur, and L. Vanderschuren, "Finite element simulation of pulsatile flow through arterial stenosis," *Journal of Biomechanics*, vol. 25, no. 10, pp. 1141–1152, 1992.

UNIVERSITÉ CATHOLIQUE DE LOUVAIN
École polytechnique de Louvain
Rue Archimède, 1 bte L6.11.01, 1348 Louvain-la-Neuve, Belgique | **www.uclouvain.be/epl**